Highly Tunable Nanostructures in a Doubly pH-Responsive Pentablock Terpolymer in Solution and in Thin Films

Jung, Florian A.; Schart, Maximilian; Bührend, Lukas; Meidinger, Elisabeth; Kang, Jia Jhen; Niebuur, Bart Jan; Ariaee, Sina; Molodenskiy, Dmitry S.; Posselt, Dorthe; Amenitsch, Heinz; Tsitsilianis, Constantinos; Papadakis, Christine M.

Highly Tunable Nanostructures in a Doubly pH-Responsive Pentablock Terpolymer in Solution and in Thin Films

Florian A. Jung, Maximilian Schart, Lukas Bührend, Elisabeth Meidinger, Jia-Jhen Kang, Bart-Jan Niebuur, Sina Ariaee, Dmitry S. Molodenskiy, Dorthe Posselt, Heinz Amenitsch, Constantinos Tsitsilianis, and Christine M. Papadakis*

Multiblock copolymers with charged blocks are complex systems that show great potential for enhancing the structural control of block copolymers. A pentablock terpolymer PMMA-*b*-PDMAEMA-*b*-P2VP-*b*-PDMAEMA-*b*-PMMA is investigated. It contains two types of midblocks, which are weak cationic polyelectrolytes, namely poly(2-(dimethylamino)ethyl methacrylate) (PDMAEMA) and poly(2-vinylpyridine) (P2VP). Furthermore, these are end-capped with short hydrophobic poly(methyl methacrylate) (PMMA) blocks in dilute aqueous solution and thin films. The self-assembly behavior depends on the degrees of ionization α of the P2VP and PDMAEMA blocks, which are altered in a wide range by varying the pH value. High degrees of ionization of both blocks prevent structure formation, whereas microphase-separated nanostructures form for a partially charged and uncharged state. While in solutions, the nanostructure formation is governed by the dependence of the P2VP block solubility of the and the flexibility of the PDMAEMA blocks on α, in thin films, the dependence of the segregation strength on α is key. Furthermore, the solution state plays a crucial role in the film formation during spin-coating. Overall, both the mixing behavior of the 3 types of blocks and the block sequence, governing the bridging behavior, result in strong variations of the nanostructures and their repeat distances.

1. Introduction

Block copolymers have gained increasing amount of attention and research interest over the past couple of decades due to their ability to self-assemble into a plethora of different structures in solution, in the bulk and in confined geometry.[1–3] Applications include, among many others, drug delivery,[4,5] injectable hydrogels,[6–8] membranes,[9,10] lithography,[11–13] sensors,[14,15] organic photovoltaics,[16] and batteries.[17,18] For many of these applications, a precise knowledge and control of their nanostructure and degree of order are imperative for best performance. A straightforward way to control the nanostructure is to change the chemical nature of the block copolymer, which alters the interaction parameter between the blocks,[19] or by changing the macromolecular topology. However, the synthesis is usually challenging and time consuming. A more promising approach is the use of multiblock polymers and of block polymers with charged segments

Dr. F. A. Jung, M. Schart, L. Bührend, E. Meidinger, J.-J. Kang, Dr. B.-J. Niebuur,[+] Prof. C. M. Papadakis
Fachgebiet Physik weicher Materie
Physik-Department
Technische Universität München
James-Franck-Str. 1, 85748 Garching, Germany
E-mail: papadakis@tum.de

The ORCID identification number(s) for the author(s) of this article can be found under https://doi.org/10.1002/adfm.202102905.

[+]Present address: INM – Leibniz Institute for New Materials, Campus D2 2, 66123 Saarbrücken, Germany

S. Ariaee, Prof. D. Posselt
IMFUFA
Department of Science and Environment
Roskilde University
P.O. Box 260, Roskilde 4000, Denmark
Dr. D. S. Molodenskiy
European Molecular Biology Laboratory
Hamburg Outstation
EMBL c/o DESY, Notkestraße 85, D-22607 Hamburg, Germany
Prof. H. Amenitsch
Institute of Inorganic Chemistry
Graz University of Technology
Stremayrgasse 9/V, Graz 8010, Austria
Prof. C. Tsitsilianis
Department of Chemical Engineering
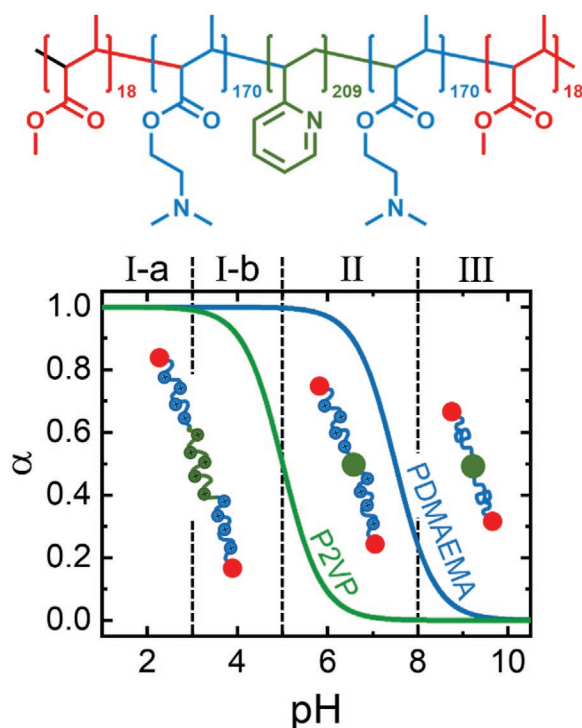University of Patras
Patras 26504, Greece

Figure 1. Chemical structure of the non-charged pentablock terpolymer and calculated degrees of ionization, α, of P2VP (green line, $pK_{a,P2VP} \cong 5.0$) and PDMAEMA (blue line, $pK_{a,PDMAEMA} \cong 7.5$) as a function of pH, using $\alpha = (1 + 10^{pH-pK^a})^{-1}$.[47] The red circles denote the hydrophobic PMMA end blocks. The regimes based on the different charge states of the pentablock terpolymer are indicated: I-a) P2VP and PDMAEMA are fully charged and hydrophilic. I-b) PDMAEMA is fully charged and P2VP is partially charged. II) P2VP is weakly charged or uncharged and hydrophobic, PDMAEMA is still highly charged and hydrophilic. III) P2VP is uncharged and hydrophobic, PDMAEMA is weakly charged or uncharged and remains hydrophilic.

which have recently received a growing interest, as these systems largely extend the range of possible structural behavior compared to the one of the well-known (neutral) diblock copolymers. Multiblock polymers can contain more than two monomer species, and the resulting enhanced functionality may provide access to novel nanostructures.[20–22] For instance, in addition to changing the chemical nature of the blocks, structural control may be gained by adjusting the sequence of the blocks.[23] Moreover, by increasing the number of blocks, an increasingly large number of block sequences can be realized, which give access to a large number of morphologies and increased functionality compared to the common diblock copolymers.[24,25] The understanding of the self-assembly behavior of multiblock polymers is, however, still in its early stages, since the multiple interaction parameters and volume fractions, in addition to the block sequences, expand the parameter space immensely.[21]

The use of charged segments in block copolymers increases the tunability of the nanostructures even further.[26,27] In diblock copolymers with charged and uncharged blocks, the additional electrostatic interactions and the presence of mobile counterions were found to alter the segregation strength between the blocks and to shift the phase boundaries.[28–33] For

example, the addition of charges to one of the blocks increases the segregation strength with the uncharged blocks, and this effect becomes more pronounced for low volume fractions of the charged block and large dielectric constant contrasts. The origin of the enhanced segregation strength are additional contributions to the free energy describing the entropy, preferential solvation, and charge correlations of the (counter)ions.[27,34–36] Charged blocks are commonly created by sulfonation or quaternization of segments, by using polyelectrolytes or by doping with salts.[37] Weak polyelectrolytes offer the additional advantage of a tunable degree of ionization due to their pH-responsiveness.[38] Multiple pH-responsive blocks give further tunability in the form of controlling charge distribution and allowing charge reversal.[39–42]

Including charged segments in multiblock polymers combines all these possibilities in a single system, which, however, accordingly becomes rather complex. While the choice of the block sequence and the volume fractions provides the basis for structural control, the electrostatic interactions may ensure strong segregation and further tuning of the nanostructure.

In the present work, we investigate a pentablock terpolymer with two chemically different types of charged blocks that are pH-responsive with a focus on the influence of the charge state of the polymer on the microphase separation and self-assembly behavior in aqueous solutions and in dry thin films. The pentablock terpolymer under investigation has a symmetric topology of the type $M_{18}D_{170}V_{209}D_{170}M_{18}$ (numbers denote the degrees of polymerization, for the chemical structures see **Figure 1**), with a central poly(2-vinylpyridine) (P2VP$_{209}$) V block and intermediate poly(2-(dimethylamino)ethyl methacrylate) (PDMAEMA$_{170}$) D blocks, which are end-capped by short poly(methyl methacrylate) (PMMA$_{18}$) M blocks. Both P2VP and PDMAEMA are weak cationic polyelectrolytes, i.e., they become positively charged at pH values below their dissociation constants pK_a of ≈ 5.0 (ref. [43]) and ≈ 7.5 (refs. [44,45]), respectively. The PMMA blocks are uncharged and hydrophobic. We chose this polymer composition since we expected that the microphase separation is mainly due to segregation between the longer PDMAEMA and P2VP blocks, which depends on their charge states, while the short PMMA blocks complete the pentablock terpolymer topology. Furthermore, the PMMA blocks stabilize the films and prevent dewetting, considering the softness of the PDMAEMA matrix. Still, the PMMA blocks were kept short to avoid kinetic freezing of the morphology.

We distinguish four main regimes of charge states, which are illustrated in Figure 1.[39] At pH values <5, below the pK_a of P2VP, both P2VP and PDMAEMA are charged (regime I). In regime I, we also distinguish the case of both blocks being fully charged (I-a, pH < 3) and the case of fully charged PDMAEMA and partially charged P2VP (I-b, 3 < pH < 5). At intermediate pH values, i.e., for 5 < pH < 8, P2VP is rather uncharged, while PDMAEMA is still rather charged (regime II). Furthermore, P2VP becomes hydrophobic, i.e., the solubility of this block in water is strongly influenced by the pH value.[46] At pH values > 8, above the pK_a of P2VP and PDMAEMA, both block types are uncharged (regime III).

In aqueous solution, micelles having a PMMA or hydrophobic P2VP core and a hydrophilic shell are expected to form above the critical micelle concentration. The shell conformation is expected to depend strongly on the pH value.

**ADVANCED
SCIENCE NEWS**

www.advancedsciencenews.com

**ADVANCED
FUNCTIONAL
MATERIALS**

www.afm-journal.de

In regimes I-a and I-b, both P2VP and PDMAEMA have a high degree of ionization and are water-soluble. Thus, the shell blocks assume a stretched conformation and are less flexible than in their neutral state.[48–51] In regime II, P2VP becomes hydrophobic and may be expected to join the micellar core to reduce contact with water. However, this would require back-folding of the PDMAEMA blocks, which is unfavorable because they are strongly charged.[52,53] Alternatively, the P2VP blocks may form a micellar core, while the PMMA blocks form dangling ends. Only in regime III, where the PDMAEMA blocks become more flexible due to a lower degree of ionization, both the P2VP blocks and the PMMA blocks may be able to form a common micellar core, which may be centrosymmetric, compartmentalized or mixed.[26] Thus, the micelles are expected to show a complex response to a change of the pH value.

While the self-assembly behavior in aqueous solution is largely governed by the water solubilities and the charge states of the blocks, this is different in thin film geometry. Here, the self-assembly behavior is mainly driven by the segment-segment interaction parameters between the blocks with additional contributions from the electrostatic interactions and the presence of counterions in regimes I-a, I-b, and II.[54] Based on theoretical work[25], the nanostructures in the uncharged state (regime III) are expected to be mainly due to the segregation between the central P2VP blocks and the intermediate PDMAEMA blocks, which form the matrix. The electrostatic interactions in regimes I-a, I-b, and II are expected to alter the segregation strength and the phase behavior, facilitated by the difference in dielectric constants of PMMA (dielectric constant $\varepsilon \approx 3$, ref. [55]) and PDMAEMA and P2VP ($\varepsilon \approx 5$, refs. [56,57]).[27,36] Furthermore, confinement and surface tension effects in the thin film geometry might induce an alignment of the nanodomains.

The investigation of both aqueous solutions and the thin films prepared from these solutions combined with a determination of the charge states of the blocks in films gives a broad view of the nanostructure formation and allows us to draw conclusions about the charge-dependent self-assembly behavior of pentablock terpolymers.

The structure of the manuscript is the following: First, the results of a structural characterization of the polymer in aqueous solution in dependence on the pH value are presented. At this, dynamic light scattering (DLS) and synchrotron small-angle X-ray scattering (SAXS) are used. Insights about the charge state of films are gained from Fourier-transform infrared spectroscopy (FTIR) measurements on films prepared from different pH values. The surface structure and the morphology of the thin films have been characterized with atomic force microscopy (AFM) and grazing-incidence small-angle X-ray scattering (GISAXS) measurements. Finally, a conclusion of the dependence of the microphase separation and self-assembly behavior on the charge state is given. In the Experimental Section, the polymer synthesis, sample preparation and experimental methods are outlined.

2. Results and Discussion

The nanostructure of the pentablock terpolymer $M_{18}D_{170}V_{209}D_{170}M_{18}$ is investigated in aqueous solutions and

in thin films in dependence on the charge states of the D and V blocks with the aim of relating the self-assembled solution structures to the nanostructures in thin films, which are prepared from these solutions. For details about the molecular characterization, the determination of the pK_a values and the sample parameters see Tables S1 and S2 and Figure S1 in the Supporting Information.

2.1. pH-Dependent Self-Assembly in Aqueous Solution

DLS measurements were performed to determine the variation of the hydrodynamic radius of particles in 0.1 wt% aqueous solutions of the pentablock terpolymer with pH. Measured intensity autocorrelation functions for pH ≤ 3.7 (regime I-a, and partially I-b in Figure 1) and pH ≥ 3.7 (regimes I-b, II, and III in Figure 1) are shown in Figure S2 in the Supporting Information, respectively. At pH 1.6, the autocorrelation function features a fast decay with decay times $\tau_{\text{fast}} \approx 0.01$–$0.1$ ms and a weak slow decay with $\tau_{\text{slow}} \approx 1$–$10$ ms. Upon increasing the pH value, the slow decay becomes more prominent at the expense of the fast decay, and at pH ≥ 3.4, only the slow decay is present. Thus, at pH < 3.4, the distribution of particle sizes is bimodal (Figure S2a, Supporting Information), while at pH ≥ 3.4, only the slow decay is observed, indicating only one type of particles. The decay shifts to smaller decay times with increasing pH, i.e., the size of the particles decreases (Figure S2b, Supporting Information).

The autocorrelation functions were analyzed by a numerical inverse Laplace transformation using the software REPES (see the Experimental Section), yielding a distribution of decay times, $A(\tau)$ (**Figure 2**a).[58] The best fits to the autocorrelation functions describe the data well (solid lines in Figure S2a,b, Supporting Information). As expected from the above discussion of the autocorrelation functions, two peaks are observed for pH < 3.4, while only a single, broad peak is present for pH ≥ 3.4. The peak related to the fast decay (left arrow in Figure 2a) shifts to smaller decay times with increasing pH value. The position of the peak associated with the slow decay (right arrow in Figure 2a) is rather constant up to pH 4.2 and shifts to smaller decay times with increasing pH values above.

Using the Stokes-Einstein equation, we calculate the hydrodynamic radius of the particles associated with the fast decay, $R_{\text{h,fast}}$, and the slow decay, $R_{\text{h,slow}}$ (Figure 2b, for details see the Experimental Section). Representative plots of the decay rate, Γ, versus the squared momentum transfer, q^2, are given in Figure S3 in the Supporting Information and show linear behavior for both types of particles, i.e., they show diffusive dynamics. Slight deviations from linear behavior at pH 6.7 and pH 8.2 are attributed to a high size dispersity which is reflected in the broad distributions in Figure 2a. $R_{\text{h,fast}}$ decreases from 13.1 ± 0.2 nm at pH 1.6 to $R_{\text{h,fast}} = 4.0 \pm 0.1$ nm at pH 2.7. In the same pH range, $R_{\text{h,slow}} \cong 250$ nm. However, due to the low amplitude of the slow decay at low pH values, the values of $R_{\text{h,slow}}$ are scattered. Between pH 3.7 and 8.2, $R_{\text{h,slow}}$ decreases from 234 ± 8 to 45 ± 2 nm.

To propose a structure based on these values, it is helpful to calculate the contour length, L_C, of the polymer. Using a monomer length $a = 0.25$ nm (length of two C-C bonds, which is appropriate for MMA, DMAEMA, and 2VP), it amounts to

**ADVANCED
SCIENCE NEWS**

www.advancedsciencenews.com

**ADVANCED
FUNCTIONAL
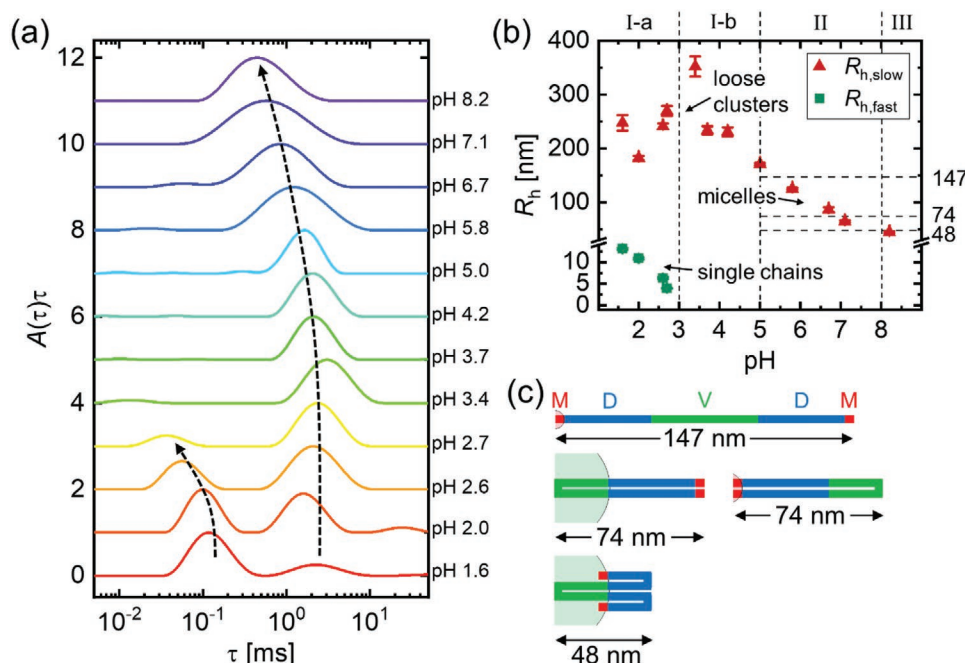MATERIALS**

www.afm-journal.de

Figure 2. a) Decay time distributions obtained from numerical inverse Laplace transformation of the DLS autocorrelation functions shown in Figure S2 in the Supporting Information. The distributions are shown in equal area representation, $A(\tau)\tau$, versus $\log(\tau)$, normalized to their highest peak and shifted upward by multiples of 1 for clarity. Arrows indicate the positions of the peaks related to the fast decay (left arrow) and the slow decay (right arrow). b) Hydrodynamic radii R_h associated with the slow and the fast decay in (a) in dependence on the pH value. Vertical dashed lines separate the charge regimes. Horizontal dashed lines indicate R_{max}. c) Schematic illustration of possible conformations of $M_{18}D_{170}V_{209}D_{170}M_{18}$ chains in a micelle and corresponding maximum micellar radii, R_{max}, under the assumption of fully stretched chains. In all cases, the leftmost block is assumed to form the micellar core. Colors represent PMMA (red), PDMAEMA (blue), and P2VP (green).

$L_C = 147$ nm. Assuming the extreme case of fully stretched chains and one PMMA end block being in the micellar core, while the other one forms a dangling end, L_C is the upper limit for the micellar radius R_{max} (Figure 2c). If both PMMA end blocks are in the same core, i.e., if the PDMAEMA-*b*-P2VP-*b*-PDMAEMA midblocks form loops, or if the P2VP blocks form the core, the maximum radius is $R_{max} = L_C/2 = 74$ nm. In the case of both PMMA blocks and the P2VP block residing in the same micellar core, the maximum radius is $R_{max} = L_{PDMAEMA}/2 + L_{P2VP}/2 = 48$ nm.

At pH ≤ 5.0, the values found for $R_{h,slow}$ are significantly larger than L_C, which indicates that large clusters or interconnected micelles are observed. The overall scattering intensity in this regime is low (Figure S4 in the Supporting Information), which indicates that the aggregates are rather loose and their number is small. Due to its small size, $R_{h,fast}$ may be attributed to single dissolved chains. At pH > 5.0, $R_{h,slow} < L_C$, indicating that single micelles with a core formed by the P2VP or the PMMA blocks are present. This is corroborated by an increase of the scattered intensity (Figure S4, Supporting Information). The decrease in size with increasing pH above pH 5.0 is attributed to the increasing hydrophobicity of P2VP and the decrease of the degree of ionization of the PDMAEMA blocks, which become less stretched. Furthermore, at high pH values, the PDMAEMA blocks become uncharged which enables the collapse of both P2VP and PMMA into the micellar core.[52] Indeed, the value of $R_{h,slow}$ at pH 8.2 (44.7 nm) is slightly below the calculated maximum size for this case (48 nm). The large

width of the decay time distributions (Figure 2a) for pH > 5.0 indicates that the different micellar architectures may coexist. Thus, with DLS, single chains, loose clusters and micelles with largely different sizes are observed in dependence on pH.

To gain insight about the shape of the particles, we performed complementary synchrotron SAXS measurements at representative pH values (**Figure 3**). Since we are mostly interested in the shape of the particles, the analysis was performed using the generalized Guinier–Porod model (one or two contributions, Equations (2) and (4), see Experimental Section). The fit parameters are summarized in Table S3 in the Supporting Information. Main parameters are the radius of gyration, R_g, the Porod exponent, p, and the shape parameter, s (see experimental section for further details).

The scattering curve at pH 2.6 (regime I-a) is well described by a single generalized Guinier–Porod model (Equation (2), Figure 3a). The resulting values of the fit parameters are $p \cong 1.2$, $s = 0$, and $R_g \cong 8.7$ nm, which indicates the presence of extended particles with a small cross-sectional radius and finite length. Combined with the DLS data, the ratio $R_g/R_{h,fast} \approx 1.4$, which is larger than the value expected for Gaussian chains (≈1.27, ref. [59]), suggests that predominantly single chains are present in the solutions at very low pH values which are rather stretched. We note that R_g is possibly related to individual P2VP and PDMAEMA blocks rather than the whole chain due to the scattering contrast between the blocks, which means that $R_g/R_{h,fast}$ is underestimated. The stretched conformation is in good
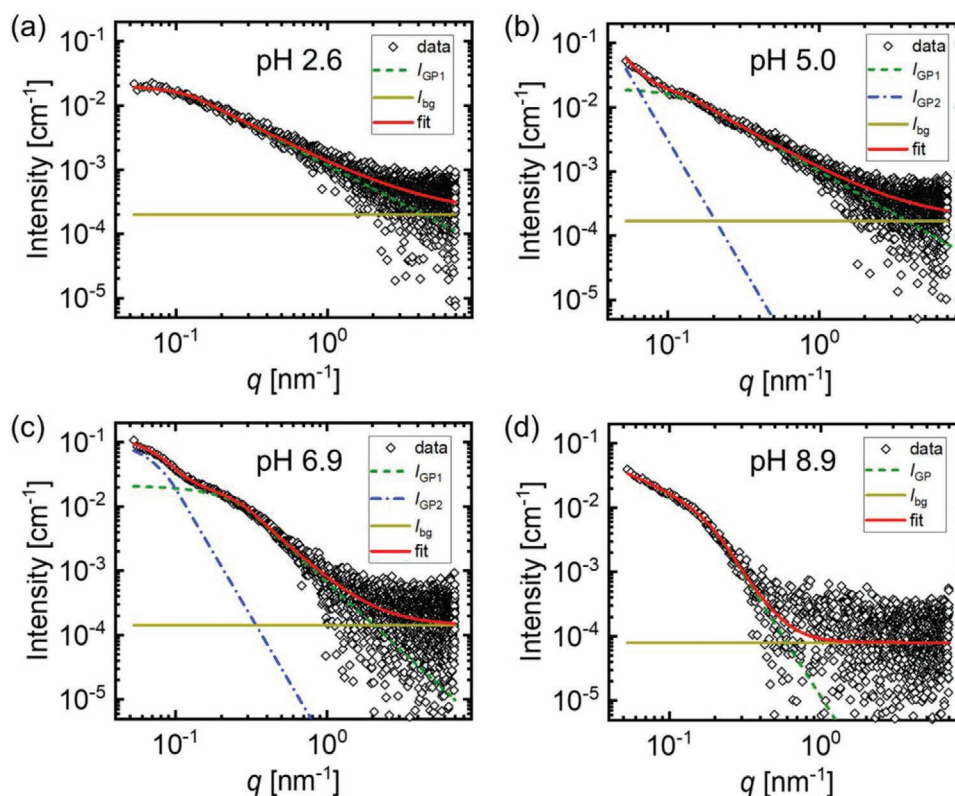
**ADVANCED
SCIENCE NEWS**

www.advancedsciencenews.com

**ADVANCED
FUNCTIONAL
MATERIALS**

www.afm-journal.de

Figure 3. SAXS curves of 0.1 wt% solutions of $M_{18}D_{170}V_{209}D_{170}M_{18}$ in H_2O at pH values of a) 2.6, b) 5.0, c) 6.9, and d) 8.9 (open symbols). Solid red lines are best model fits using Equation (2) (pH 2.6 and 8.9) or Equation (4) (pH 5.0 and 6.9). Additional colored lines indicate the different contributions to the fitting model (see legend). For more details about the models, see text and the Supporting Information.

agreement with previous results on P2VP homopolymers at low pH values.[50]

At pH 5.0 (regime I-b), the scattering curve is similar to the one at pH 2.6 for $q > 0.15$ nm^{-1}, i.e., chain scattering is still present ($I_{GP1}(q)$), but features an additional intensity upturn toward smaller q values (Figure 3b). The upturn is modeled by a second generalized Guinier–Porod model ($I_{GP2}(q)$, Equation (4)). The fit parameters of the model describing the chain scattering are $p_1 \cong 1.3$, $s_1 = 0$, and $R_{g,1} \cong 8.1$ nm, which indicates that the chains are still stretched, but less than at pH 2.6. For describing the upturn, the parameters are fixed at the following values: $p_2 = 4.0$, $s_2 = 0$, and $R_{g,2} = 130$ nm, i.e., this term describes the scattering from large clusters. The parameters are fixed since the absence of a plateau at low q values does not allow to determine s_2 and $R_{g,2}$, and the accessible q-range is too small to allow fitting p_2 reliably. We note that, while $R_{g,2}$ is approximated from the DLS data at pH 5.0 as $R_{g,2} = 0.77 \times R_{h,slow} \cong 130$ nm (using the ratio $R_g/R_h = 0.77$ for solid spheres), all values $R_{g,2} > R_{min} \cong \pi/q_{min} \cong 60$ nm give equally good fits. To conclude, at pH 5.0, large clusters are present which, as evidenced by the significant chain scattering contribution, are rather loose.

At pH 6.9 (regime II), the scattering curve consists of two shoulders at $q \approx 0.08$ nm^{-1} and $q \approx 0.2$ nm^{-1} (Figure 3c) and is well described by a model with two generalized Guinier–Porod terms (Equation (4)). The fit parameters obtained are $p_1 \cong 2.2$, $s_1 = 0$, and $R_{g,1} \cong 5.4$ nm and $p_2 = 4.0$, $s_2 = 0$, and $R_{g,2} \cong 23.9$ nm. The first term follows the q^{-2} dependence formulated by Debye and therefore describes the scattering from Gaussian chains.[60]

The second term is related to the overall size of the particles, which have a spherical shape. Thus, the particles are spherical micelles with a corona of swollen Gaussian chains. This is corroborated by the ratio $R_{g,2}/R_{h,slow} \cong 0.35$, which is indicative of micelles with spherical core and strongly swollen corona.[61]

The scattering curve at pH 8.9 (regime III) has a single shoulder at $q \approx 0.15$ nm^{-1} (Figure 3d). It is well described by a single generalized Guinier–Porod model (Equation (2)) with fit parameters $p \cong 3.7$, $s \cong 0.9$, and $R_g \cong 7.3$ nm, indicating cylindrical particles with a cross-sectional radius R_g and an almost smooth surface, which are attributed to worm-like micelles. The absence of a clear plateau at low q values does not allow to extract an overall radius of gyration $R_{g,2}$, which might have been compared to the DLS results. However, assuming once more $R_{g,2} > R_{min} \cong 60$ nm and $R_{h,slow} < 45$ nm gives $R_{g,2}/R_{h,slow} > 1.3$ which is indicative of extended wormlike micelles.

Based on the DLS and SAXS measurements, we propose the self-assembled solution structures schematically shown in **Figure 4**. In regime I-a, for pH < 3, at which P2VP and PDMAEMA are fully ionized (Table S2, Supporting Information), strong stretching and electrostatic repulsion of the chains prevent aggregation, and most chains are molecularly dissolved. This agrees with results from molecular simulations on hydrophobically end-capped polyelectrolytes, which show a decrease of the micellar aggregation number with increasing degree of ionization.[62] In our case, the fraction of hydrophobic PMMA segments is small (≈6% compared to
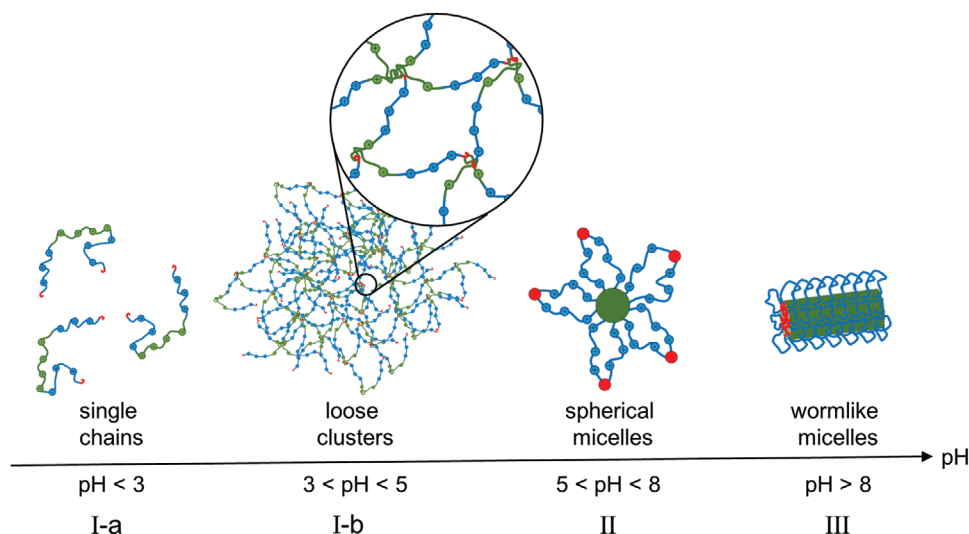
Figure 4. Schematic drawing of the proposed most prominent self-assembled structures of $M_{18}D_{170}V_{209}D_{170}M_{18}$ in aqueous solution at different pH values. From left to right: dissolved single chains; large loose clusters; spherical micelles; wormlike micelles. Colors indicate PMMA (red), PDMAEMA (blue), and P2VP (green). The structures are not drawn to scale.

≈67% in ref. [62]), which promotes the complete dissolution of the polymer at high degrees of ionization of PDMAEMA and P2VP.[63] As evidenced by the presence of the weak slow decay in DLS, few large and loose clusters (network-like) are present as well. At larger pH values in regime I-b, for $3 < pH < 5$, these clusters become prominent, and almost no dissolved chains are present. The clusters presumably form due to intramolecular and intermolecular interactions of the hydrophobic entities (the short PMMA blocks and few uncharged P2VP units).[39] Their formation is facilitated by the strongly stretched conformation of the PDMAEMA blocks and the deprotonation of the P2VP blocks (Table S2, Supporting Information).

In regime II, for $5 < pH < 8$, the P2VP block is uncharged and hydrophobic, which enhances the overall hydrophobicity of the pentablock terpolymer and promotes self-assembly of the PMMA and P2VP blocks. The PDMAEMA blocks still have a high degree of ionization and are stretched, which prevents the hydrophobic P2VP domains from merging with the PMMA domains. These effects promote the formation of spherical micelles with i) hydrophobic cores of PMMA and satellites of P2VP or ii) with cores of P2VP and satellites of PMMA.[52,63] Due to the much larger volume fraction of P2VP, case (ii) is the most likely one.

In regime III, for $pH > 8$, the PDMAEMA blocks become uncharged and flexible. Thus, they can fold, allowing both the PMMA and P2VP blocks to join the micellar core, resulting in wormlike micelles with two loops per chain. Since the PMMA end blocks are very short compared to the P2VP blocks, it is likely that the P2VP blocks form the center of the core, which is surrounded by a layer of PMMA blocks.[26]

Thus, the self-assembly of the MDVDM pentablock terpolymer depends strongly on its charge state. The observed structures include single chains, loose clusters, spherical micelles, and wormlike micelles with different chain conformations. The average sizes of these structures vary strongly and change by almost a factor of four.

2.2. Charge State of the Films

The question arises if the charge states (which strongly affect the self-assembled nanostructures) in aqueous solution can be directly transferred into dry films. At this, FTIR measurements on films of thicknesses of several micrometers which were prepared by drop-casting from aqueous solutions having pH values of 3.9 (regime I-a), 5.1, 6.1, and 7.2 (regime II), and 8.3 (regime III), were performed to determine the charge state of dry films from the pentablock terpolymer.

Figure 5a shows the FTIR spectra over a broad range of wavenumbers. The absorbances were normalized to the height of the strong C=O peak at ≈1729 cm^{-1} to account for thickness variations of the drop-cast films. The C=O peak was chosen since it has a clear signal, due to its presence in both the PMMA blocks and the PDMAEMA blocks, and this functional group is not affected by a change of the pH value; thus, the peak height is proportional to the amount of sample that is illuminated.[64] The spectra are rather complex, owing to the multiple blocks and functional groups in the system, especially in the fingerprint region at wavenumbers smaller than 2000 cm^{-1}. However, differences in the spectra are clearly seen in the wavenumber regions 3600–3100 cm^{-1}, where the absorbance increases with decreasing pH value, and 2900–2300 cm^{-1}, where several peaks disappear, while others appear at lower pH values. The latter show a particularly strong increase in absorbance at pH values between 8.3 and 7.2 and between 5.1 and 3.9. In the fingerprint region, especially between 1650–1550 cm^{-1}, changes occur. Figure 5b and c shows expanded regions of the spectra, and these are discussed in the following.

From 3600 to 3100 cm^{-1}, a broad peak is observed, which is attributed to O−H stretching vibrations from water molecules absorbed by the films from ambient air.[65] The N−H$^+$ stretching vibrations, which are expected to be present in charged PDMAEMA and P2VP, also fall in this region.[66] It is, however, difficult to distinguish the contributions from each
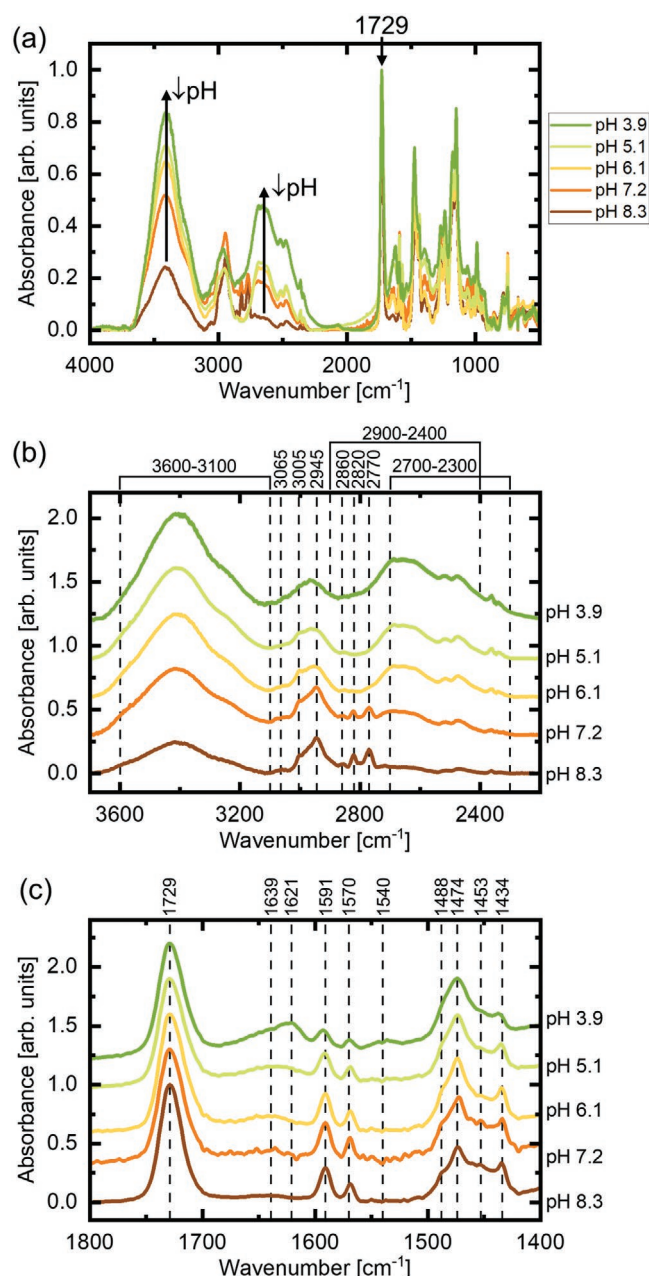
**ADVANCED
SCIENCE NEWS**

www.advancedsciencenews.com

**ADVANCED
FUNCTIONAL
MATERIALS**

www.afm-journal.de

Figure 5. a) Normalized FTIR spectra of films drop-cast from aqueous solutions at the pH values given on the right. Arrows indicate changes occurring with decreasing pH value. b) Zoom of the wavenumber range 3700–2200 cm⁻¹. c) Zoom of the wavenumber range 1800–1400 cm⁻¹. The positions of characteristic peaks are given in cm⁻¹ and are indicated by dashed lines. For clarity, the spectra in (a) and (b) are shifted upward by multiples of 0.3. The unshifted spectra are shown in Figure S5 in the Supporting Information.

peak and to determine their relative contributions in this wavenumber range. Still, in both cases, this is a first indication of the protonation of PDMAEMA and/or P2VP, which increases their hydrophilicity and water uptake.

The three peaks at ≈3065, ≈3005, and ≈2945 cm⁻¹ are assigned to C−H stretching vibrations of aromatic as well as CH_3 and CH_2 groups and do not show any significant

pH-responsive behavior.[67] At pH 8.3, three peaks are present at ≈2860, ≈2820, and ≈2770 cm⁻¹, which have a lower amplitude at pH 7.2 and vanish at pH values below. These are attributed to the N−$(CH_3)_2$ stretching vibrations present in the tertiary amine group of PDMAEMA.[68,69] Their absence at low pH values may be explained by the protonation of this group which suppresses the stretching vibrations.[70] The peak assignment is confirmed by FTIR measurements of PDMAEMA homopolymer films drop-cast from pH values of 1.7, 5.9, and 9.3. The spectra are shown in Figure S6 in the Supporting Information. Indeed, the three peaks at ≈2860, ≈2820, and ≈2770 cm⁻¹ are clearly visible in the spectra of the homopolymer films at pH 9.3, but are absent at the lower pH values.

Between 2700 and 2300 cm⁻¹, a set of peaks is observed, which increase in magnitude with decreasing pH value. They are a strong indication of the presence of a tertiary amine salt, which is formed by PDMAEMA.[71] The magnitude of these peaks increases strongly from pH 8.3 to pH 7.2, i.e., around the pK_a of PDMAEMA. From pH 7.2 to pH 5.1, their magnitude increases only slightly, because PDMAEMA is already almost fully protonated. The same behavior is observed in the PDMAEMA homopolymer films (Figure S6a, Supporting Information).

At pH 3.9, a broad peak between ≈2900 and ≈2400 cm⁻¹ overlaps with the peaks described above. This peak can be attributed to the formation of pyridine hydrochloride in the reaction of P2VP with HCl.[67,72] For comparison, reference FTIR spectra from literature of pyridine and pyridine hydrochloride in this wavenumber range are given in Figure S7a in the Supporting Information.

The strong peak at 1729 cm⁻¹ is associated to free (non-hydrogen bonded) C=O stretching vibrations,[64,73] which are present in both PDMAEMA and PMMA. Since this peak is unchanged with pH, it was used for normalization of the spectra. A weak peak at ≈1639 cm⁻¹ is attributed to bending vibrations of water.[74] The peak is also present in the spectra of the PDMAEMA homopolymer at low pH values, which indicates that the enhanced water solubility of PDMAEMA is one reason for the absorption of water (Figure S6b, Supporting Information).

At ≈1621 and ≈1540 cm⁻¹, two peaks appear at pH values of 5.1 and 3.9. In contrast, at ≈1591, ≈1570, and ≈1434 cm⁻¹, peaks are present which decrease in magnitude with decreasing pH value. The former peaks are attributed to pyridine hydrochloride and the latter ones to free pyridine, which indicates the protonation of the pyridine groups of P2VP at pH values of 5.1 and below.[72,75–79] Similar trends are also observed in the reference spectra in Figure S7b in the Supporting Information.

The peaks at ≈1488, ≈1474, and ≈1453 cm⁻¹ are attributed to vibrational modes in PDMAEMA, since they are prominently present in the homopolymer spectra (Figure S6b, Supporting Information). However, these peaks do not show any significant changes with the pH value.

Thus, we conclude the following charge state of the films depending on the pH value during film preparation: At pH values of 8.3 and 7.2, i.e., close to the pK_a of PDMAEMA, P2VP is fully uncharged and PDMAEMA is weakly charged. Between pH 7.2 and pH 5.1, PDMAEMA becomes fully protonated while P2VP remains unprotonated. At pH 3.9, both PDMAEMA and
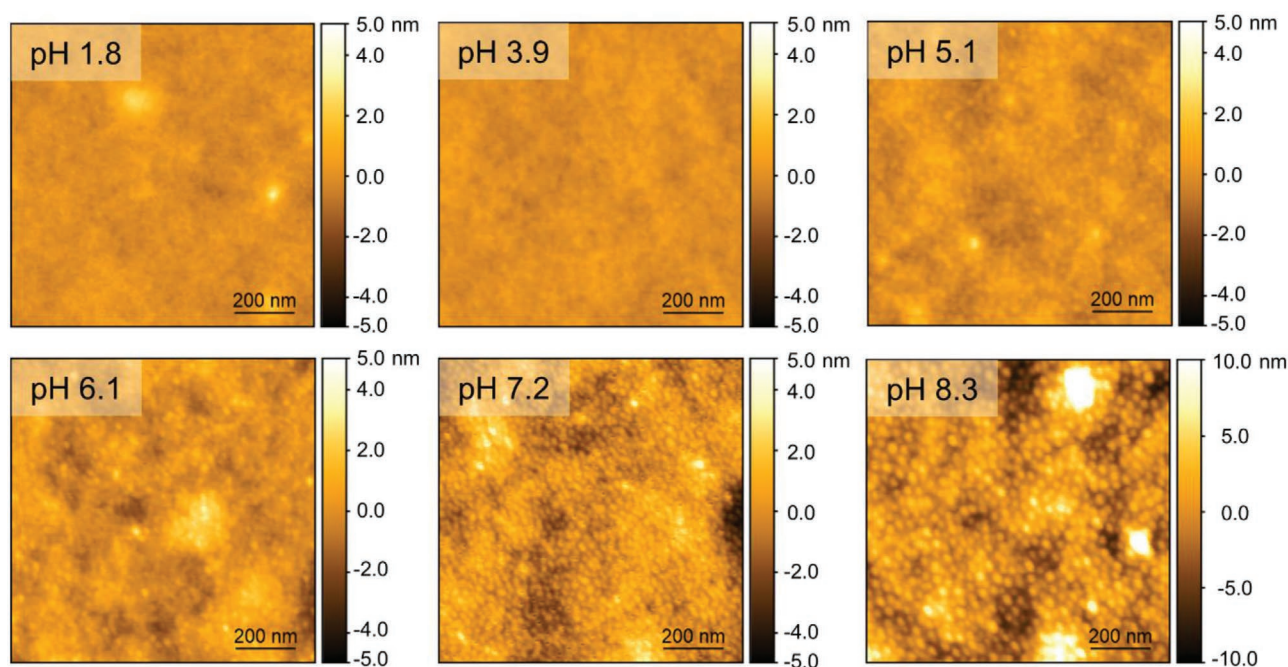
ADVANCED
SCIENCE NEWS
www.advancedsciencenews.com

ADVANCED
FUNCTIONAL
MATERIALS
www.afm-journal.de

Figure 6. AFM height images of films prepared from the pH values given. The scale bar is 200 nm, and the color scales are given on the right of each image.

P2VP are fully protonated. In particular, the formation of tertiary amine salts and pyridine salts, i.e., complexation of the charged groups with counterions, is observed. Thus, the pH regimes sketched in Figure 1 for aqueous solutions translate also to thin films, i.e., the charge state of the dry polymer films is highly tunable by varying the pH value during film preparation.

2.3. Surface Nanostructure of Films Prepared at Different pH Values

Thin films were prepared by spin-coating from solutions having pH values of 1.8 (regime I-a), 3.9 (regime I-b), 5.1, 6.1, and 7.2 (regime II), and 8.3 (regime III). To investigate the surface nanostructure and thereby gain information on the self-assembly behavior of the terpolymers, AFM measurements were performed, and height images of all films are shown in **Figure 6**. The corresponding phase images are shown in Figure S8 in the Supporting Information. For the films prepared from solutions having pH values of 1.8 and 3.9, the surfaces are rather homogeneous, i.e., no microphase-separated nanostructure is identified. At a pH value of 5.1, a dot-like nanostructure is found, which may be assigned to standing cylinders, which protrude from the film surface, or to spheres. While the dots have a characteristic size and distance, no long-range order is present. At pH values of 6.1 and 7.2, the same nanostructure is observed, becoming more pronounced with increasing pH value, i.e., the dots protrude more and more from the film surface, as the pH increases. At a pH value of 8.3, the radius of the dots is larger than at pH values of 6.1 and 7.2, and their protrusion height has significantly increased (note the enlarged color scale of the AFM height image compared to the other pH values). Additionally, at a pH value of 8.3, large aggregates are present on the film surface, which appear as large, bright spots in the AFM height image. The phase images are consistent with the interpretation of the height images. Furthermore, the dots appear bright in the phase images which suggest that they are formed by the stiffer P2VP or PMMA blocks rather than the soft PDMAEMA blocks.[80]

For a more quantitative characterization, several height profiles were extracted for each image and were analyzed by hand, focusing on the distance between the dots and their height. The height profiles and details of their analysis are given in Figures S9–S11, in the Supporting Information, and the resulting distances and heights of the cylinders are shown in **Figure 7**. The reported errors are standard deviations of several height profiles. At pH 1.8 and 3.9, the height profiles are nearly flat and do not show any nanostructure. At pH 5.1–8.3, modulations become visible. The average distance decreases from ≈35 nm at pH 5.1 to ≈29 nm at pH 6.1 and 7.2, while the average protrusion height increases from ≈0.5 to ≈0.7 nm. At pH 8.3, the distance has increased to ≈38 nm and the protrusion height to ≈2 nm. The large aggregates at pH 8.3 have an approximate radius of ≈30 nm and a height of ≈20–25 nm (Figure S11, Supporting Information).

The behavior of the dot-dot distance and the protrusion height falls into regimes which correspond to the main regimes introduced in Figure 1. In regimes I-a and I-b (pH < 5), no microphase separation is observed, and the films are disordered. In regime II (5 < pH < 8), the films microphase-separate into a spherical or cylindrical nanostructure. In this regime, the dot-dot distance decreases significantly with increasing pH value, and the dots protrude from the film surface with a protrusion height which increases slightly with pH. In regime III (pH > 8), both, the dot-dot distance and the height of the protrusions are significantly larger compared to regime II. Additionally, large aggregates are present in regime III.
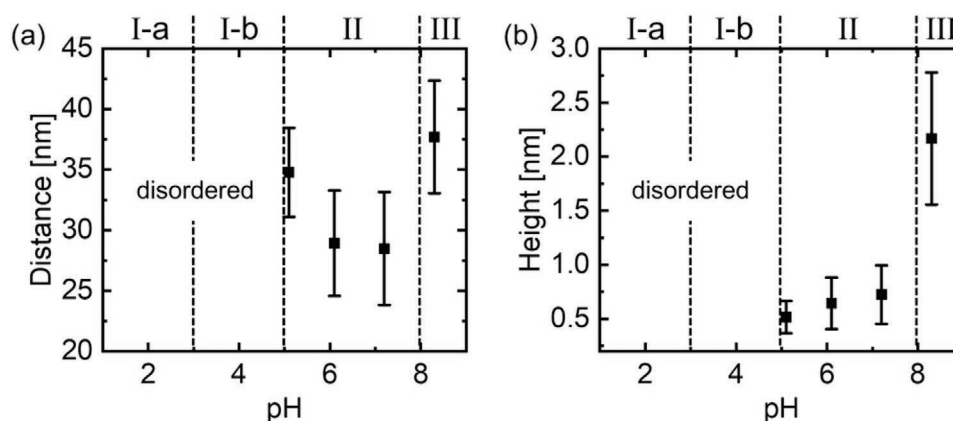
Figure 7. Average dot-dot distance and protrusion height determined from the AFM height images in Figure 7 as a function of the pH value during film preparation. Dashed lines separate the charge regimes shown in Figure 1.

2.4. pH-Dependent Inner Nanostructure of the Thin Films

Since AFM probes only the film surface and cannot distinguish between the spherical and cylindrical morphologies, GISAXS experiments were performed to gain insight into the inner nanostructure of the films.[81] 2D GISAXS patterns of films prepared from aqueous solutions at pH values of between 2.1 and 8.2, as well as one of a film prepared from a methanol solution are shown in **Figure 8** ($q_y > 0$). Best matching simulations of the GISAXS patterns, which are discussed below, are shown as well ($q_y < 0$). Methanol was chosen for the preparation of one film since, in this solvent, P2VP and PDMAEMA are expected to have a lower degree of dissociation than in water, which reflects the neutral charge state in regime III. An aqueous solution at high pH value cannot be used since the polymer becomes insoluble at pH > 9. Differently from regime III, methanol is a good solvent for uncharged P2VP, while water is a non-solvent. All 2D patterns feature the specularly reflected beam, which is partially covered by the beamstop (marked with red crosses in Figure 8). Moreover, strong scattering along $q_y = 0$ is present, which is due to off-specular diffuse scattering from the rough film and substrate surfaces. Weak diffuse scattering is overall present as a background signal and can be attributed to air scattering and/or scattering from the sample holder (see ref. [54] for a detailed analysis of the background contributions in the GISAXS patterns). At $q_z \approx 0.3$ nm^{-1}, the Yoneda band is located (marked Y in Figure 8), i.e., the region of enhanced intensity between the critical angles of the polymer film ($\alpha_{c,film} \approx 0.17°$) and the Si substrate ($\alpha_{c,Si} \approx 0.22°$). Details about the calculation of the critical angles are given in Table S4 in the Supporting Information.

At pH 2.1, no additional features are present in the 2D pattern, i.e., no indication of nanostructure inside the polymer film is found. At pH 4.1, a weak Bragg peak (marked B in Figure 8) is visible at $q_y^* \approx 0.18$ nm^{-1}, which is an indication of microphase separation with a characteristic repeat distance $D = 2\pi/q_y^* \approx 35$ nm. At pH 4.8, in addition to the Bragg peak, a Bragg rod (marked R in Figure 8) extends along q_z and is slightly bent inward (toward $q_y = 0$). This rod is indicative of a vertical alignment of the nanostructure, which we assume to be cylinders, in agreement with the corresponding AFM

images.[82,83] For a spherical nanostructure, the rod would be absent, as was shown by us previously.[54] Up to pH 7.1, these features remain, and the q_y position of the Bragg peak increases to ≈0.30 nm^{-1} corresponding to $D \approx 21$ nm. At pH 7.1 and 8.2, two additional features appear: strong scattering at small q_y values especially near the specular peak, which also leads to an apparent broadening of the off-specular diffuse scattering, and an additional scattering peak below the specular peak at $q_z \approx 0.2$ nm^{-1} (marked P in Figure 8). Due to the small q_y values, these features may be attributed to large scattering objects, e.g., aggregates. The 2D pattern of the film prepared from methanol is similar to the one at pH 5.2.

Based on these observations and the AFM results, we chose a cylindrical morphology to simulate the 2D GISAXS patterns, expecting the cylinders to be formed by P2VP and/or PMMA embedded in a matrix of PDMAEMA. A schematic drawing of the simulation model is shown in **Figure 9**a, for details see Figures S12–S14 in the Supporting Information. Standing cylinders with radius R_{pro} and small height H_{pro} are positioned on top of a film to model the protrusions observed with AFM. The protrusions are distributed laterally like a radial paracrystal with an average distance D_{pro} and a Gaussian probability distribution function with a half-width w_{pro}. Similarly, larger cylinders with radius R_{agg} and height H_{agg} on top of the film model the aggregates observed at elevated pH values. For the aggregates, no correlation term was needed, i.e., they are not correlated with each other. The inner structure of the polymer film is modeled by standing cylinders with radius R_{cyl} and height H_{cyl} which are randomly positioned normal to the film surface but are distributed laterally like a radial paracrystal with an average distance D_{cyl} and a Gaussian probability distribution function with a half-width w_{cyl}. The parameters of the cylinders modeling the protrusions and the inner structure are independent from each other to account for possible deviations between these two structures in the films. Both the radius and the height of the three types of cylinders are size distributed according to Gaussian distribution functions with relative widths $\sigma_H/H = \sigma_R/R = 0.2$, where σ_i are the standard deviations of the distributions. Weighting terms account for the scattering contrast and relative amounts of the three types of cylinders.

Horizontal line cuts at the Yoneda band position of the experimental 2D patterns (open symbols) and best fit simulations
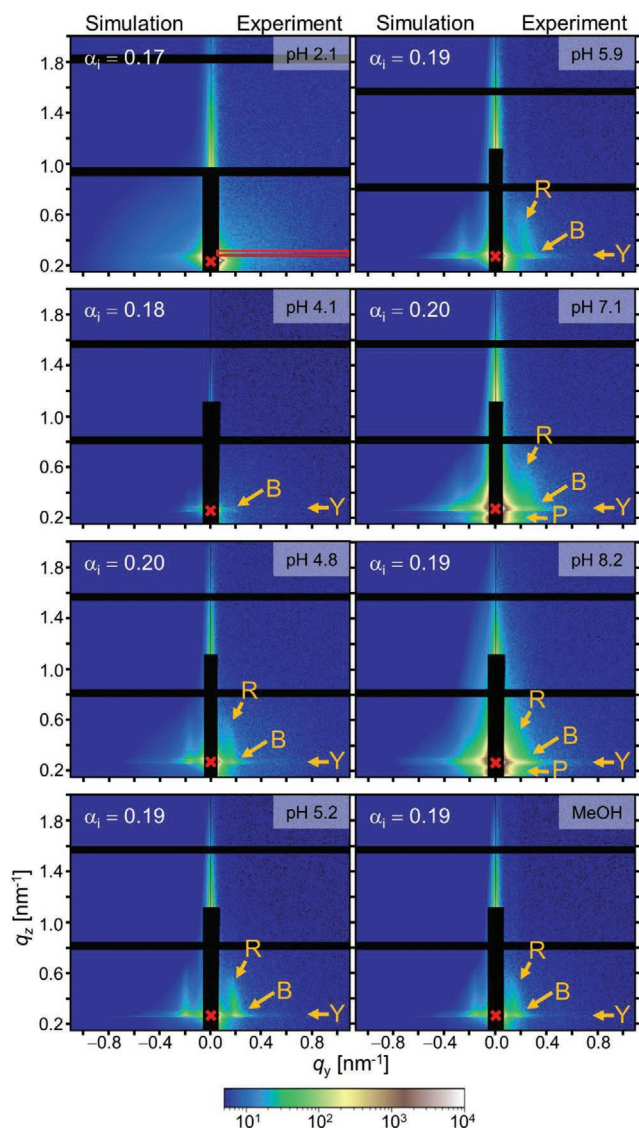
Figure 8. 2D GISAXS patterns from the experiment ($q_y > 0$) and from simulations ($q_y < 0$) of films prepared from aqueous solution of different pH values and from methanol. The incident angles of the X-rays, α_i, are indicated. The position of a typical horizontal line cut used for fitting is indicated with a red box in the pattern at pH 2.1. The position of the specular peak is indicated with a red cross on top of the beam stop. Orange arrows indicate positions of Yoneda band (Y), main Bragg peak (B), scattering rod (R), and additional scattering peaks (P). The scale bar at the bottom gives the logarithmic color scale. The GISAXS setup for the sample prepared at a pH value of 2.1 was different from the one described in the Experimental Section in that a sample-to-detector distance of 1668 mm was used.

(red solid lines) are shown in Figure 9b. Similarly, vertical line cuts at the position of the Bragg peak (for pH 2.1, a position comparable to the other patterns was chosen) are shown in Figure 9c. Additional line cuts can be found in Figure S15 in the Supporting Information. We first discuss the experimental cuts. At pH 2.1, no Bragg peak is visible in the horizontal cut, as expected from the qualitative inspection of the 2D pattern (Figure 8). Additionally, the intensity in the Yoneda band is

low in the vertical cuts (Figure 9c) which further hints at the absence of a nanostructure, which, if present, would lead to enhanced intensity in this region. Starting at pH 4.1, a weak Bragg peak appears in the horizontal cuts which becomes more pronounced with increasing pH and shifts to larger q_y values until pH 7.1 (indicated with a green dashed arrow in Figure 9b). In the vertical cuts, the intensity in the Yoneda band increases with increasing pH. At pH 7.1 and pH 8.2, the Bragg peak is rather broad and low in intensity and shifts to smaller q_y values with increasing pH. In the vertical cuts, the additional scattering peak (P) observed in the 2D patterns is clearly visible at $q_z \approx 0.2$ nm^{-1} (marked with green arrows). For the film prepared from a methanol solution, the line cuts show similar behavior to pH 5.2, which was also the case for the 2D scattering patterns.

Overall, the fitting procedure outlined by us previously is followed.[54] The contributions to the scattering pattern of respectively the cylinders modeling the protrusions, the aggregates and the inner structure are each most prominent in distinct regions of the patterns and can thus be distinguished. Best-fit simulations model the experimental scattering patterns in great detail (Figure 8) and describe all features in the characteristic line cuts (Figure 9b,c; Figure S15, Supporting Information). The structural parameters of the simulations are summarized in **Table 1**.

The aggregates are present in the films prepared at pH values of 7.1 and 8.2 and have a radius of $R_{agg} \approx 30$ nm and a height of $H_{agg} \approx 25$ nm. These values agree well with the AFM results at pH 8.2 (Figure S11, Supporting Information). It is interesting to note that the GISAXS results show the presence of aggregates on the film surface at pH 7.1, while they are absent in the AFM image at pH 7.2 (Figure 6). This is likely due to the small area of the film that is probed with AFM, while with GISAXS, a much larger area is probed.

Protrusions with heights of ≈0.8, ≈1.0, and ≈2.5 nm are used in the simulations at pH values of 5.9, 7.1, and 8.2, respectively. At pH values ≤ 5.2 and for the film prepared from methanol, their height is low, and their volume is presumably too small to give sufficient scattering intensity; therefore, they are neglected in the simulations. The pH dependence of the protrusion height at pH 5.9–8.2 agrees with the AFM results (Figure 7b). At pH values of 5.9 and 7.1, the radius of the protrusions is set to ≈6 nm and the distance between protrusions to ≈25 and ≈20 nm, respectively. However, due to the small total volume, their contribution to the scattering pattern is too weak for an accurate determination. At pH 8.2, their contribution is more prominent and values of R_{pro} and D_{pro} are determined to be ≈8 and ≈40 nm, respectively. The high value of D_{pro} compared to the lower pH values also agrees with the AFM results.

The protrusions presumably form due to the high glass transition temperatures of PMMA ($T_g \cong 105$ °C, ref. [84]) and P2VP ($T_g \cong 104$ °C, ref. [43]), which, during spin-coating and solvent removal, become glassy and immobile while the non-glassy PDMAEMA matrix ($T_g \cong 10$ °C, ref. [85]) continues to collapse.[86,87] The effect is more pronounced at higher pH values due to the hydrophobicity of P2VP which makes water a poor plasticizer and promotes faster immobilization. The aggregates presumably originate from kinetically frozen micelles in the solution, which have highly hydrophobic mixed PMMA/P2VP cores. In the film prepared from methanol, the aggregates and
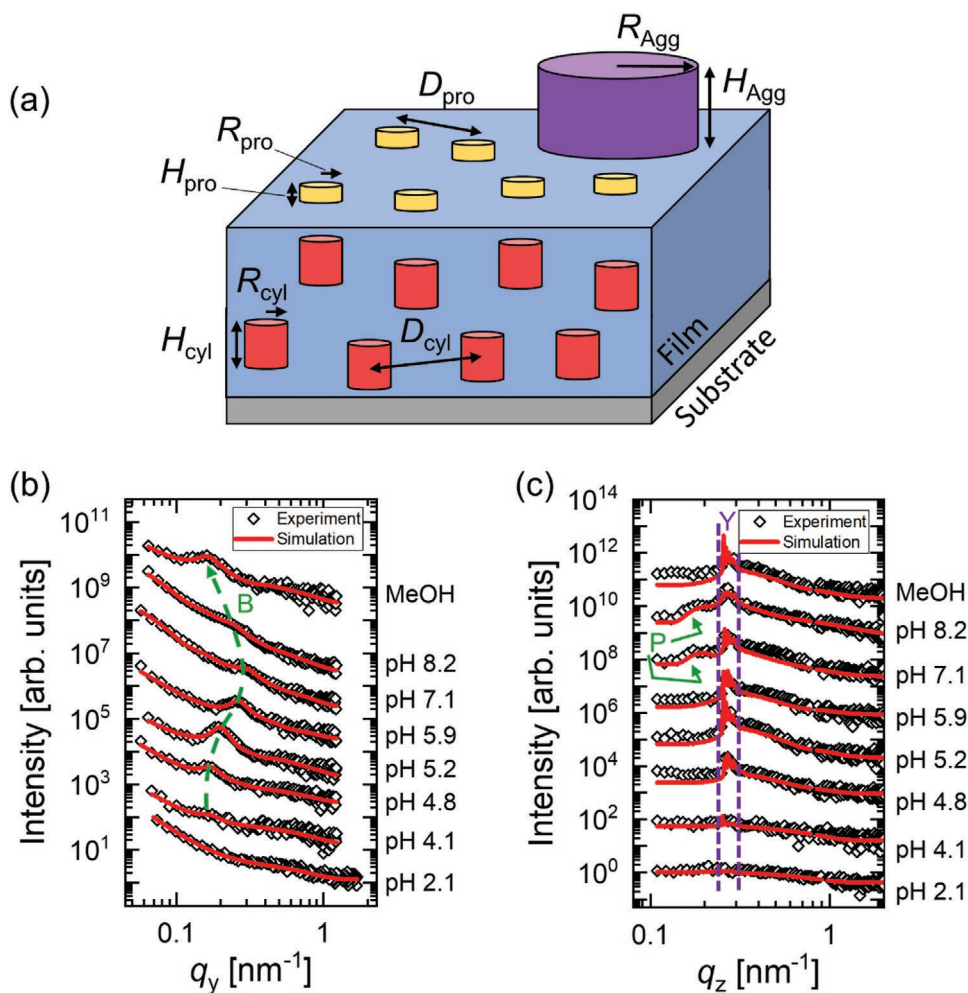
Figure 9. a) Model of the film nanostructure in the GISAXS simulations: cylindrical protrusions of small height (≈1–2 nm; yellow) and large aggregates (also cylindrical; purple) are positioned on top of a polymer film. Inside the film, standing cylinders of larger height (≈10 nm; red color) are positioned. b) Horizontal line cuts at the Yoneda band position and c) vertical line cuts at the position of the Bragg peak from the 2D GISAXS patterns shown in Figure 8 for the given pH values and for methanol. Open symbols: experiments. Solid red lines: results from simulations. For clarity, the data are shifted vertically, and only every third data point is shown. In (b), the change of the position of the Bragg peak (B) is indicated with a green dashed arrow. The appearance of a scattering peak (P) below the specular peak at high pH values is indicated with green arrows, and the Yoneda band (Y) is indicated with purple dashed lines in (c).

Table 1. Structural parameters of films extracted from the 2D GISAXS simulations.

Parameter	pH 2.1	pH 4.1	pH 4.8	pH 5.2	pH 5.9	pH 7.1	pH 8.2	MeOH
R_{cyl} [nm]	–	10.7 ± 4.2	9.5 ± 0.7	9.0 ± 0.4	5.6 ± 0.2	6.1 ± 0.5	8.0 ± 1.4	10.5 ± 0.6
H_{cyl}[a] [nm]	–	10	10	10	10	10	10	10
D_{cyl} [nm]	–	34.3 ± 4.8	34.8 ± 1.2	30.1 ± 0.5	22.7 ± 0.4	19.5 ± 1.0	25.0 ± 1.5	35.1 ± 1.5
w_{cyl} [nm]	–	8.4 ± 2.8	8.6 ± 0.8	6.5 ± 0.4	5.2 ± 0.3	5.3 ± 0.5	5.6 ± 1.3	9.5 ± 0.9
R_{pro}[a] [nm]	–	–	–	–	6	6	8	–
H_{pro}[a] [nm]	–	–	–	–	0.8	1.0	2.5	–
D_{pro}[a] [nm]	–	–	–	–	25	20	40	–
w_{pro}[a] [nm]	–	–	–	–	5	5	30	–
R_{agg}[a] [nm]	–	–	–	–	–	30	30	–
H_{agg}[a] [nm]	–	–	–	–	–	25	25	–

[a]Parameters adjusted by hand to best describe the experimental data, but not part of the fitting routine.

**ADVANCED
SCIENCE NEWS**

www.advancedsciencenews.com

**ADVANCED
FUNCTIONAL
MATERIALS**

www.afm-journal.de

protrusions are absent since methanol acts as a plasticizing solvent for P2VP.

The radius and distance of the cylinders describing the inner structure of the films are compiled in **Figure 10**. At pH 2.1, the films have no inner structure, which, together with the lack of surface nanostructure found with AFM, implies that the whole film is disordered. At pH 4.1, R_{cyl} and D_{cyl} are ≈10.7 and ≈34.3 nm, respectively, however, with large uncertainties. With increasing pH value, they decrease to ≈6.1 and ≈19.6 nm, respectively, at pH 7.1. At pH 8.2, R_{cyl} and D_{cyl} increase to ≈8.0 and ≈25.0 nm, respectively, and have values of ≈10.5 and ≈35.1 nm, respectively, for the film prepared from a methanol solution. In all microphase-separated films, a height of 10 nm is found to best describe the Bragg rods present in the experimental scattering patterns. The slight inward bend of the rods indicates that the cylinders in the films are not entirely vertical, but that some sections of the cylinders are tilted. Therefore, the value of 10 nm is expected to represent the average length of the vertical sections of the cylinders.

Again, the behavior of R_{cyl} and D_{cyl} can be separated into regimes, which correlate with the regimes introduced in Figure 1. In regime I-a (pH < 3), the films are disordered, and in regime I-b (3 < pH < 5), the films are weakly ordered. In regimes II and III, the films are microphase-separated and feature an inner nanostructure of mostly vertical cylinders. The structure sizes decrease with increasing pH value in regime II by nearly a factor of two and increase in regime III. This

behavior is consistent with the behavior of the surface nanostructure found with AFM (Figure 7a).

The proposed microphase-separated structures of the pentablock terpolymer in thin films are shown in **Figure 11** in dependence on the pH value. In regime I-a and I-b, the films are disordered or weakly ordered. Presumably, this is due to the high degree of ionization of both P2VP and PDMAEMA, which promotes mixing of all blocks to maximize the counterion entropy.[27]

At the lower pH range in regime II (pH ≈ 5–6), cylinders are formed which we attribute to the P2VP blocks, while the matrix is a mixture of PDMAEMA and PMMA blocks. The assignment is based on the volume fractions of the blocks and agrees with theoretical work on the self-assembly of pentablock terpolymers.[25] Because PDMAEMA is fully charged and P2VP is partially charged, PMMA is expected to have a strong tendency to segregate from both blocks.[27,54] However, due to its low volume fraction (f_{PMMA} ≈ 0.05), it mixes with the neighboring PDMAEMA blocks, as predicted by ref. [25]. At the higher pH range in regime II (pH ≈ 6–8), the P2VP blocks are fully uncharged, and the PMMA blocks are more likely to mix with them than with the charged PDMAEMA matrix, thus cylinders of mixed P2VP/PMMA blocks are formed. Due to the chain architecture, the cylinders are bridged by PDMAEMA blocks which explains the low cylinder–cylinder distance in this pH range. Presumably, the solution state (see Figure 4) during film preparation facilitates these nanostructures: The fully charged PDMAEMA blocks are strongly stretched and cannot be folded, so that mixing of P2VP and PMMA is only possible if the blocks are located in separate domains which are connected by the PDMAEMA blocks, forming a network-like structure. This explanation is corroborated by the high film thickness of the films prepared at these pH values, which is significantly higher compared to the other pH values (see Table S2 in the Supporting Information). The network-like structures increase the viscosity of the solution during spin-coating, which leads to a higher film thickness.[88]

In regime III, we propose that the cylinders are formed by mixed P2VP/PMMA blocks, but with a lower degree of connectivity, i.e., the PDMAEMA blocks form loops rather than bridges. This explains the higher cylinder–cylinder distances observed (Figure 10b). The reason is the presence of micelles with two loops per chain in the solutions, which is adopted in the films during spin-coating.

Thus, the film nanostructure depends on both the charge state and the solution state during film preparation. We note that the film nanostructures are possibly not in equilibrium, due to the high glass transition temperatures of PMMA and P2VP. However, the soft PDMAEMA matrix allows significant rearrangements, as evidenced by the formation of strongly aligned cylinders from the micellar solutions.
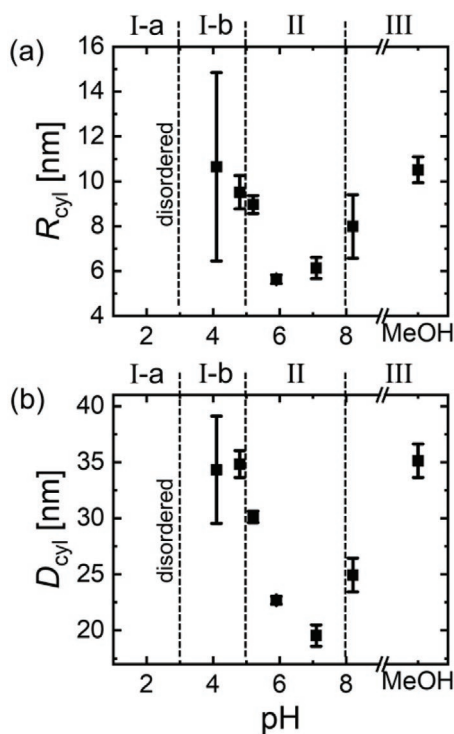

Figure 10. Selected parameters of the cylinders describing the inner structure of the polymer films obtained from best fit simulations of the GISAXS patterns: a) Radius of cylinders inside polymer film, R_{cyl}. b) Cylinder–cylinder distance, D_{cyl}. Dashed lines separate the charge regimes shown in Figure 1.

3. Conclusion

The self-assembly of the doubly pH-responsive pentablock terpolymer $PMMA_{18}$-b-$PDMAEMA_{170}$-b-$P2VP_{209}$-b-$PDMAEMA_{170}$-b-$PMMA_{18}$
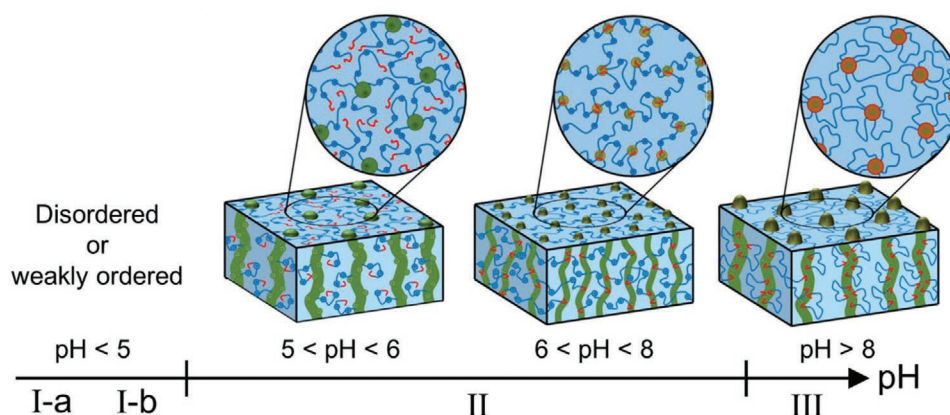
Figure 11. Schematic drawing of the microphase-separated structures in thin films depending on the charge state (pH value during film preparation). Colors indicate PMMA (red), PDMAEMA (blue), and P2VP (green). Ionized PDMAEMA and P2VP blocks are indicated with charge symbols. Counterions are present in the films with charged PDMAEMA blocks, but are not explicitly drawn for clarity.

in aqueous solution and in thin film geometry is investigated in dependence on the charge state of the polymer. The PDMAEMA and P2VP blocks are weak cationic polyelectrolytes with different dissociation constants, which allows to tune the charge state by a variation of the pH value and hence to distinguish three regimes. Furthermore, compared to triblock copolymers with only one weak polyelectrolyte central block, such as PMMA-*b*-PDMAEMA-*b*-PMMA,[63] the charge distribution along the polymer chain is not random, but segmental. We find that this has a remarkable influence on the self-assembly behavior of the polymer and offers great control.

In solution, the polymer is fully dissolved at low pH values (regime I-a, pH < 3), whereas at slightly higher pH values (regime I-b (3 < pH < 5), loose clusters form. This is presumably due to the high degrees of ionization of both the PDMAEMA and the P2VP blocks, which prevent aggregation of the short, hydrophobic PMMA end blocks. In regime II (5 < pH < 8), where P2VP is weakly charged or uncharged, aggregation takes place. Loose clusters or micelles with cores of PMMA or P2VP are formed. The rather stretched PDMAEMA blocks prevent merging of these two blocks, and the spherical micelles with cores of P2VP have satellites of hydrophobic short PMMA blocks. In regime III (pH > 8), the uncharged PDMAEMA blocks become flexible and both the P2VP and the PMMA blocks can enter the micellar core, which is accompanied by a double PDMAEMA loop formation per chain and a transition to wormlike micelles. Therefore, the micellar architecture is widely tunable, ranging from star-like micelles (dangling ends) to flower-like micelles and micelles with double loops. Depending on the conditions, the sizes of these micelles differ by a factor of 3–4 and are in the range of ≈40–130 nm. Therefore, in solution, this type of pentablock terpolymers could be useful for delivery applications which require two release mechanisms.

With FTIR measurements, it is shown that the charge state in solution, which is adjusted by variation of the pH value, can be transferred into thin films. Therefore, block copolymers with blocks from several weak polyelectrolytes allow to easily tune the charge state of dry films by adjusting the pH value during film preparation. While this preparation method requires water as a solvent, i.e., it is limited to water-soluble polymers, this

method of preparation of charged block copolymer films is versatile and is complementary to methods based on the ionization of blocks during the polymer synthesis, e.g., by sulfonation of blocks,[29,32] or on post-treatments of films.[89]

In thin films, the pentablock terpolymer is disordered in regime I-a or weakly ordered in regime I-b, and assumes a cylindrical morphology in regimes II and III. The cylinders predominantly have a vertical orientation and are presumably formed by P2VP and/or PMMA which reside in a PDMAEMA matrix. The radius and distance of the cylinders depend strongly on the charge state and vary between ≈6–10 and ≈35–20 nm, respectively. These strong differences are proposed to originate from different arrangements of the blocks, i.e., the presence of pure or mixed cylinders and the way these are bridged. Therefore, by variation of the charge state, the characteristic size of the nanostructures in charged pentablock terpolymer thin films can be tuned in a wide range. Due to the strong segregation strength between charged and uncharged blocks, it is expected that the characteristic sizes can be further reduced by lowering the degree of polymerization of the pentablock terpolymer, while maintaining microphase separation.

In summary, the use of pH-responsive blocks in a pentablock terpolymer allowed us to control the charge state and to characterize the dependence of the self-assembly behavior on the electrostatic interactions. By investigating both solutions and thin films, insight into the structure formation was obtained. The results contribute to the understanding of multiblock copolymers containing charged segments and point to potentially very interesting applications in batteries and membranes, due to small and tunable feature sizes of charged systems.

4. Experimental Section

Polymer Synthesis and Characterization: The PMMA-*b*-PDMAEMA-*b*-P2VP-*b*-PDMAEMA-*b*-PMMA pentablock terpolymer was synthesized by "living" anionic polymerization in a one pot, three-step reaction using sodium tetraphenyl diisobutane as a bifunctional organometallic initiator and sequential monomer addition. The reaction was carried out in anhydrous tetrahydrofuran (THF) solution under argon atmosphere. 2-Vinyl pyridine was firstly polymerized at −78 °C, followed by successive polymerization of

2-(dimethylamino) ethyl methacrylate and methyl methacrylate, −65 °C. In each step, part of the reaction medium was sampled out for the purpose of characterization. The reaction was terminated by the addition of a few drops of methanol. The terpolymer was precipitated in cold hexane, re-dissolved in benzene, filtered and freeze-dried.

The pentablock and its precursors (P2VP, PDMAEMA-*b*-P2VP-*b*-PDMAEMA) were characterized in terms of molecular weight and molecular polydispersity by size exclusion chromatography (SEC) using polystyrene standards. The analysis was carried out using two PL gel columns of different pore size and RI-detector. The mobile phase was 1% triethylamine solution in THF and the flow rate 0.5 mL min⁻¹. The monomer composition was determined by nuclear magnetic resonance (¹H NMR) using a Bruker AC-400 spectrometer using CDCl₃ as deuterated solvent. Provided that SEC gives apparent molecular weights the degree of polymerization of each block was estimated from the M_w of the P2VP precursor (SEC) and the weight fraction of the monomers (¹H NMR). The characterization data are gathered in Table S1 in the Supporting Information.

Sample Preparation: Aqueous solutions were prepared by dissolving the polymer in demineralized H₂O at concentrations of 0.1 wt% (DLS and SAXS on solutions), or 3 wt% (films) and by stirring the mixture overnight. The 0.1 wt% solutions for DLS were additionally filtered with a 0.8 μm mixed cellulose ester syringe filter and again stirred overnight. The reason different concentrations were chosen are the specific requirements of the characterization methods.

The pH value of such prepared solutions was measured using a Metrohm 826 pH meter with a glass electrode and had in all cases values of 5.1–5.4. Afterward, the pH of the solution was adjusted to lower pH values using small amounts of 1 M HCl and to higher values using 2 or 1 M NaOH.

Solutions in methanol (MeOH) were prepared by dissolving the polymer at a concentration of 2 wt% and by stirring the mixture overnight.

A titration curve is shown in Figure S1 in the Supporting Information. Two shoulders can be identified which are attributed to equivalence points of PDMAEMA and P2VP, respectively. Since the shoulders overlap partially and the one related to PDMAEMA is poorly defined, no attempt to determine the pK_a values from the titration curve was made. Instead, the literature values of p$K_{a,PDMAEMA} \approx 7.5$ (refs. [44,45]) and p$K_{a,P2VP} \approx 5.0$ (ref. [43]) are used for this work. The features of the curve are consistent with these values.

Si(100) wafers (SilChem GmbH, Germany) of size 1.5 × 1.5 cm² were acid cleaned (85 mL H₂O: 70 mL H₂O₂: 165 mL H₂SO₄) at 80 °C for 15 min. Afterward, the wafers were rinsed with water several times and then stored in deionized water until use.

Thin films were prepared by 4 spin coating steps, each at 4000 rpm and lasting 30 s. Firstly, the Si wafers were removed from the water storage bath and spin dried. Secondly, acetone was used to remove any remaining organic residues. Thirdly, water was applied to make the surface hydrophilic. Fourthly, the 3 wt% polymer solutions were used. Afterward, the films were subjected to vacuum at room temperature overnight to remove residual solvent. With this method, homogeneous, dry polymer films were obtained.

For FTIR measurements, thicker films were prepared by drop casting of the 3 wt% polymer solutions after the first three spin coating steps described above and letting the films dry for several days under ambient conditions. The film thicknesses were at least several micrometers.

An overview of the calculated degrees of ionization of P2VP and PDMAEMA of all solutions as well as the thicknesses of the films prepared for GISAXS measurements, is given in Table S2 in the Supporting Information.

Dynamic Light Scattering (DLS): DLS measurements were performed using a LS Spectrometer (LS Instruments, Fribourg, Switzerland). The polarized HeNe laser (Thorlabs, Dachau, Germany) has a maximum power output of 21 mW and a wavelength of 632.8 nm. A goniometer arm allows for multiangle measurements and two avalanche photodiode (APD) detectors were used for photon detection. The temperature of the sample was controlled by placing it in a heatable bath of index matching solvent (mixed *trans*- and *cis*-decalin) and was kept constant

at 30 °C. The temperature was controlled using a Julabo CF31 Cryo-Compact Circulator (JULABO, Seelbach, Germany). As sample cells, cylindrical glass cuvettes with outer diameter 5 mm and wall thickness 0.4 mm were used. The scattering angle θ was varied between 45° and 120°. At each angle, 10 normalized intensity autocorrelation functions, $g_2(q,\tau)$, were recorded for 30 s using a multi-tau correlator and were subsequently averaged after removing outliers. $q = 4\pi n/\lambda \times \sin(\theta/2)$ is the momentum transfer, where n is the refractive index of the solvent and λ the wavelength of the laser light.

To analzye the autocorrelation curves, a numerical inverse Laplace transformation was performed, which calculates the distribution of decay times, $A(\tau)$, using the software REPES.[58,90] A probability to reject of 0.5 was used. One or two decays were typically observed. At each scattering angle, weight average decay times of the fast decay, τ_{fast} (from pH 1.6–3.4), and the slow decay, τ_{slow} (in the entire pH range), were extracted and transformed into decay rates using $\Gamma_i = 1/\tau_i$, where i stands for the fast or slow decay. Diffusion coefficients, D_i, were obtained from linear fits to Γ_i versus q^2 plots, following the relation $D_i = \Gamma_i/q^2$. The hydrodynamic radii were determined using the Stokes-Einstein equation

$$R_{h,i} = \frac{k_B T}{6\pi\eta D_i} \tag{1}$$

where k_B is Boltzmann's constant, T the temperature, and η the viscosity of water.

Small-Angle X-Ray Scattering (SAXS): Synchrotron SAXS measurements were performed at beamline P12 at the European Molecular Biology Laboratory (EMBL) at DESY, Hamburg.[91] The wavelength was $\lambda = 0.12398$ nm. The scattered intensity was recorded using a PILATUS 6M detector (pixel size 172 μm) at sample-to-detector distances of 3.0 m. The temperature was fixed at 20 °C, and for each measurement 50–80 frames (exposure time 45 ms) were collected and subsequently averaged while the solution was continuously flowing through a thin-walled quartz capillary with a diameter of 1.8 mm.[92] Azimuthally averaged scattering curves were corrected for background scattering from the quartz capillary and H₂O and for transmission by the automated data processing pipeline SASFLOW and are given as a function of the scattering vector $q = 4\pi/\lambda \times \sin(\theta/2)$ (θ is the scattering angle).[93] Water was used as a standard to convert the intensities to absolute units.

The scattering curves were analyzed using the following model

$$I(q) = I_{GP}(q) + I_{bg} \tag{2}$$

$I_{GP}(q)$ is the generalized Guinier–Porod model which gives information about the size and shape of scattering particles. I_{bg} is a constant background arising from systematic beamline noise as well as a negligible mismatch between the pure H₂O buffer and the polymer solution. $I_{GP}(q)$ is given by[94]

$$I_{GP}(q) = \begin{cases} \dfrac{G}{q^s}\exp\left(\dfrac{-q^2 R_g^2}{3-s}\right), & q \leq q_1 \\[3mm] G\exp\left(\dfrac{-q_1^2 R_g^2}{3-s}\right)q_1^{(p-s)}q^{-p}, & q \geq q_1 \end{cases} \tag{3}$$

$$q_1 = \frac{1}{R_g}\left[\frac{(p-s)(3-s)}{2}\right]^{1/2}$$

G is a scaling factor, R_g is the radius of gyration, p is the Porod exponent, and s is the shape parameter. $3 < p < 4$ is indicative of surface fractals (e.g., rough surfaces), while $p < 3$ indicates mass fractals, including Gaussian chains for $p \cong 2$.[95] $p \cong 1$ indicates rigid rods. By the shape

**ADVANCED
SCIENCE NEWS**

www.advancedsciencenews.com

**ADVANCED
FUNCTIONAL
MATERIALS**

www.afm-journal.de

parameter, globular ($s = 0$) and rod-like ($s = 1$) particles can be distinguished.

For the scattering curves at pH 5.0 and 6.9, a second Guinier–Porod term was added which accounts for a second type of structure

$$I(q) = I_{GP1}(q) + I_{GP2}(q) + I_{bg} \tag{4}$$

Model fits were performed using SasView 4.2.2 employing a least-square algorithm.[96]

Atomic Force Microscopy (AFM): The surface structure of spin-coated films was probed using an MFP-3D AFM (Oxford Instruments Asylum Research, Santa Barbara, U.S.A.). A tip with a curvature of 7 nm was used and was mounted on a cantilever OMCL-AC240TS-R3 (Asylum Research). Height profiles were obtained by operating the device in intermittent-contact mode with a drive frequency of 65–81 kHz and a scan rate of 0.7–1.2 Hz. The measured AFM images were leveled and corrected for a polynomial background using the software Gwyddion v2.55.[97]

Fourier-Transform Infrared Spectroscopy (FTIR): FTIR spectra were recorded with a Bruker Equinox FTIR spectrometer equipped with a deuterated triglycine sulfate detector under ambient conditions. A spectral resolution of 1 cm^{-1} was used, and the signal was averaged over 256 scans. The wavenumber range was set from 450 to 4000 cm^{-1}. Spectra were corrected for a baseline and atmospheric compensation of CO_2 and H_2O using the software OPUS provided by Bruker.

Grazing-Incidence Small-Angle X-Ray Scattering (GISAXS): GISAXS experiments were performed at the Austrian SAXS beamline at the Elettra Sincrotrone Trieste (ELETTRA).[98] The X-ray wavelength, λ, was 0.155 nm and the beam size 1.0 mm × 0.15 mm ($H \times V$). The detector was a PILATUS3 1M (981 × 1043 pixels) with a pixel size of 172 μm at a sample-to-detector distance of 1951 mm, which resulted in a q-resolution of 3.6×10^{-3} nm^{-1} pixel^{-1}. The q-range was calibrated using silver behenate. To prevent the intense reflected beam from damaging the detector, a rod like beam stop was used. Incident angles α_i were set to values between 0.17° and 0.20°, which are between the critical angles of the polymer film ($\alpha_{c,film} \approx 0.17°$) and the Si substrate ($\alpha_{c,Si} = 0.23°$). For data analysis, GISAXS simulations were performed using the software BornAgain 1.16.[99,100] The simulations explicitly account for scattering from the surface roughness of the polymer film and the substrate, and background contributions from the aluminum sample holder. The nanostructure of the polymer films was modeled by placing particles inside the films (buried particles) or on top (surface structure). More details about the simulations and the fitting procedure are given in our previous publication.[54]

Supporting Information

Supporting Information is available from the Wiley Online Library or from the author.

Acknowledgements

Conflict of Interest

The authors declare no conflict of interest.

Data Availability Statement

Research data are not shared.

[1] F. S. Bates, G. H. Fredrickson, *Phys. Today* **1999**, *52*, 32.

[2] C. M. Bates, F. S. Bates, *Macromolecules* **2017**, *50*, 3.

[3] H. Feng, X. Lu, W. Wang, N.-G. Kang, J. W. Mays, *Polymers* **2017**, *9*, 494.

[4] G. S. Kwon, M. L. Forrest, *Drug Dev. Res.* **2006**, *67*, 15.

[5] A. Pitto-Barry, N. P. E. Barry, *Polym. Chem.* **2014**, *5*, 3291.

[6] C. T. Huynh, M. K. Nguyen, D. S. Lee, *Macromolecules* **2011**, *44*, 6629.

[7] C. Chassenieux, C. Tsitsilianis, *Soft Matter* **2016**, *12*, 1344.

[8] C. M. Papadakis, C. Tsitsilianis, *Gels* **2017**, *3*, 3.

[9] S. P. Nunes, *Macromolecules* **2016**, *49*, 2905.

[10] Y. Zhang, N. E. Almodovar-Arbelo, J. L. Weidman, D. S. Corti, B. W. Boudouris, W. A. Phillip, *npjClean Water* **2018**, *1*, 2.

[11] J. G. Kennemur, L. Yao, F. S. Bates, M. A. Hillmyer, *Macromolecules* **2014**, *47*, 1411.

[12] C. M. Bates, M. J. Maher, D. W. Janes, C. J. Ellison, C. G. Willson, *Macromolecules* **2014**, *47*, 2.

[13] J. Kwak, A. K. Mishra, J. Lee, K. S. Lee, C. Choi, S. Maiti, M. Kim, J. K. Kim, *Macromolecules* **2017**, *50*, 6813.

[14] Y. Acikbas, F. Taktak, R. Capan, C. Tuncer, V. Bütün, M. Erdogan, *IEEE Sens. J.* **2018**, *18*, 5313.

[15] S. Z. Bas, C. Cummins, A. Selkirk, D. Borah, M. Ozmen, M. A. Morris, *ACS Appl. Nano Mater.* **2019**, *2*, 7311.

[16] D. Heinrich, M. Hufnagel, C. R. Singh, M. Fischer, S. Alam, H. Hoppe, T. Thurn-Albrecht, M. Thelakkat, in *Elementary Processes in Organic Photovoltaics* (Ed: K. Leo), Springer International Publishing, Basel **2017**, p. 157.

[17] N. S. Wanakule, J. M. Virgili, A. A. Teran, Z.-G. Wang, N. P. Balsara, *Macromolecules* **2010**, *43*, 8282.

[18] R. Bouchet, S. Maria, R. Meziane, A. Aboulaich, L. Lienafa, J.-P. Bonnet, T. N. T. Phan, D. Bertin, D. Gigmes, D. Devaux, R. Denoyel, M. Armand, *Nat. Mater.* **2013**, *12*, 452.

[19] C. Sinturel, F. S. Bates, M. A. Hillmyer, *ACS Macro Lett.* **2015**, *4*, 1044.

[20] V. Sfika, C. Tsitsilianis, A. Kiriy, G. Gorodyska, M. Stamm, *Macromolecules* **2004**, *37*, 9551.

[21] F. S. Bates, M. A. Hillmyer, T. P. Lodge, C. M. Bates, K. T. Delaney, G. H. Fredrickson, *Science* **2012**, *336*, 434.

**ADVANCED
SCIENCE NEWS**

www.advancedsciencenews.com

**ADVANCED
FUNCTIONAL
MATERIALS**

www.afm-journal.de

[22] V. P. Beyer, J. Kim, C. R. Becer, *Polym. Chem.* **2020**, *11*, 1271.

[23] S. L. Perry, C. E. Sing, *ACS Macro Lett.* **2020**, *9*, 216.

[24] M. W. Matsen, R. B. Thompson, *J. Chem. Phys.* **1999**, *111*, 7139.

[25] H.-H. Liu, C.-I. Huang, A.-C. Shi, *Macromolecules* **2015**, *48*, 6214.

[26] C. Tsitsilianis, Y. Roiter, I. Katsampas, S. Minko, *Macromolecules* **2008**, *41*, 925.

[27] C. E. Sing, J. W. Zwanikken, M. Olvera de la Cruz, *Nat. Mater.* **2014**, *13*, 694.

[28] M. J. Park, N. P. Balsara, *Macromolecules* **2008**, *41*, 3678.

[29] M. Goswami, B. G. Sumpter, T. Huang, J. M. Messman, S. P. Gido, A. I. Isaacs-Sodeye, J. W. Mays, *Soft Matter* **2010**, *6*, 6146.

[30] X. Wang, M. Goswami, R. Kumar, B. G. Sumpter, J. Mays, *Soft Matter* **2012**, *8*, 3036.

[31] C. R. Stewart-Sloan, B. D. Olsen, *ACS Macro Lett.* **2014**, *3*, 410.

[32] J. Shim, F. S. Bates, T. P. Lodge, *Nat. Commun.* **2019**, *10*, 2108.

[33] S. T. Russell, R. Raghunathan, A. M. Jimenez, K. Zhang, S. D. Brucks, C. Iacob, A. C. West, O. Gang, L. M. Campos, S. K. Kumar, *Macromolecules* **2020**, *53*, 548.

[34] I. Nakamura, Z.-G. Wang, *Soft Matter* **2012**, *8*, 9356.

[35] C. E. Sing, J. W. Zwanikken, M. Olvera de la Cruz, *Phys. Rev. Lett.* **2013**, *111*, 168303.

[36] C. E. Sing, J. W. Zwanikken, M. Olvera de la Cruz, *J. Chem. Phys.* **2015**, *142*, 034902.

[37] W. S. Loo, M. D. Galluzzo, X. Li, J. A. Maslyn, H. Jeung Oh, K. I. Mongcopa, C. Zhu, A. A. Wang, X. Wang, B. A. Garetz, N. P. Balsara, *J. Phys. Chem. B* **2018**, *122*, 8065.

[38] G. Kocak, C. Tuncer, V. Bütün, *Polym. Chem.* **2017**, *8*, 144.

[39] J. F. Gohy, S. Antoun, R. Jérôme, *Macromolecules* **2001**, *34*, 7435.

[40] S. L. Canning, T. J. Neal, S. P. Armes, *Macromolecules* **2017**, *50*, 6108.

[41] Y. W. Harn, Y. He, Z. Wang, Y. Chen, S. Liang, Z. Li, Q. Li, L. Zhu, Z. Lin, *Macromolecules* **2020**, *53*, 8286.

[42] M. Wang, K. He, J. Li, T. Shen, Y. Li, Y. Xu, C. Yuan, L. Dai, *J. Biomater. Sci., Polym. Ed.* **2020**, *31*, 849.

[43] J. G. Kennemur, *Macromolecules* **2019**, *52*, 1354.

[44] F. A. Plamper, M. Ruppel, A. Schmalz, O. Borisov, M. Ballauff, A. H. E. Müller, *Macromolecules* **2007**, *40*, 8361.

[45] F. A. Plamper, C. V. Synatschke, A. P. Majewski, A. Schmalz, H. Schmalz, A. H. E. Müller, *Polymers* **2014**, *59*, 66.

[46] Z. Posel, Z. Limpouchová, K. Šindelka, M. Lísal, K. Procházka, *Macromolecules* **2014**, *47*, 2503.

[47] L. Nová, F. Uhlík, P. Košovan, *Phys. Chem. Chem. Phys.* **2017**, *19*, 14376.

[48] H. J. Limbach, C. Holm, *J. Phys. Chem. B* **2003**, *107*, 8041.

[49] A. V. Dobrynin, M. Rubinstein, *Prog. Polym. Sci.* **2005**, *30*, 1049.

[50] Y. Roiter, S. Minko, *J. Am. Chem. Soc.* **2005**, *127*, 15688.

[51] D. G. Mintis, M. Dompé, M. Kamperman, V. G. Mavrantzas, *J. Phys. Chem. B* **2020**, *124*, 240.

[52] C. Tsitsilianis, N. Stavrouli, V. Bocharova, S. Angelopoulos, A. Kiriy, I. Katsampas, M. Stamm, *Polymers* **2008**, *49*, 2996.

[53] M.-T. Popescu, C. Tsitsilianis, C. M. Papadakis, J. Adelsberger, S. Balog, P. Busch, N. A. Hadjiantoniou, C. S. Patrickios, *Macromolecules* **2012**, *45*, 3523.

[54] F. A. Jung, D. Posselt, D.-M. Smilgies, P. A. Panteli, C. Tsitsilianis, C. S. Patrickios, C. M. Papadakis, *Macromolecules* **2020**, *53*, 6255.

[55] F. Namouchi, H. Smaoui, N. Fourati, C. Zerrouki, H. Guermazi, J. J. Bonnet, *J. Alloys Compd.* **2009**, *469*, 197.

[56] A. V. Krayev, R. V. Talroze, *Polymers* **2004**, *45*, 8195.

[57] S. P. Samant, C. A. Grabowski, K. Kisslinger, K. G. Yager, G. Yuan, S. K. Satija, M. F. Durstock, D. Raghavan, A. Karim, *ACS Appl. Mater. Interfaces* **2016**, *8*, 7966.

[58] J. Jakeš, *Collect. Czech.. Chem. Commun.* **1995**, *60*, 1781.

[59] A. Chremos, J. F. Douglas, *MRS Adv.* **2016**, *1*, 1841.

[60] P. Debye, *J. Phys. Chem.* **1947**, *51*, 18.

[61] A. S. Lee, V. Bütün, M. Vamvakaki, S. P. Armes, J. A. Pople, A. P. Gast, *Macromolecules* **2002**, *35*, 8540.

[62] M. Ghelichi, N. T. Qazvini, *Soft Matter* **2016**, *12*, 4611.

[63] G. T. Gotzamanis, C. Tsitsilianis, S. C. Hadjiyannakou, C. S. Patrickios, R. Lupitskyy, S. Minko, *Macromolecules* **2006**, *39*, 678.

[64] C. F. Huang, F. C. Chang, *Polymers* **2003**, *44*, 2965.

[65] J.-J. Max, C. Chapados, *J. Chem. Phys.* **2009**, *131*, 184505.

[66] M. M. Coleman, K. H. Lee, D. J. Skrovanek, P. C. Painter, *Macromolecules* **1986**, *19*, 2149.

[67] D. Lin-Vien, N. B. Colthup, W. G. Fateley, J. G. Grasselli, *The Handbook of Infrared and Raman Characteristic Frequencies of Organic Molecules*, Academic Press, San Diego **1991**.

[68] M. S. Agashe, C. I. Jose, *J. Chem. Soc., Faraday Trans. 2* **1977**, *73*, 1232.

[69] A. Angelini, C. Fodor, W. Yave, L. Leva, A. Car, W. Meier, *ACS Omega* **2018**, *3*, 18950.

[70] J.-J. Yin, F. Wahid, Q. Zhang, Y.-C. Tao, C. Zhong, L.-Q. Chu, *Macromol. Mater. Eng.* **2017**, *302*, 1700079.

[71] B. C. Smith, *Spectroscopy* **2019**, *34*, 30.

[72] M. Kątcka, T. Urbański, *Bull. Acad. Pol. Sci., Ser. Sci., Math., Astron. Phys.* **1964**, *12*, 615.

[73] D. Li, J. Brisson, *Polymers* **1998**, *39*, 793.

[74] M. Ludvigsson, J. Lindgren, J. Tegenfeldt, *Electrochim. Acta* **2000**, *45*, 2267.

[75] D. Cook, *Can. J. Chem.* **1961**, *39*, 2009.

[76] M. Puterman, J. L. Koenig, J. B. Lando, *J. Macromol. Sci., Part B: Phys.* **1979**, *16*, 89.

[77] Y. L. Yang, Y. Kou, *Chem. Commun.* **2004**, *4*, 226.

[78] N. V. Salim, N. Hameed, Q. Guo, *J. Polym. Sci., Part B: Polym. Phys.* **2009**, *47*, 1894.

[79] Y. Zhang, P. Bi, J. Wang, P. Jiang, X. Wu, H. Xue, J. Liu, X. Zhou, Q. Li, *Appl. Energy* **2015**, *150*, 128.

[80] S. N. Magonov, V. Elings, M.-H. Whangbo, *Surf. Sci.* **1997**, *375*, L385.

[81] G. Renaud, R. Lazzari, F. Leroy, *Surf. Sci. Rep.* **2009**, *64*, 255.

[82] M. Li, K. Douki, K. Goto, X. Li, C. Coenjarts, D. M. Smilgies, C. K. Ober, *Chem. Mater.* **2004**, *16*, 3800.

[83] F. F. Lupi, T. J. Giammaria, G. Seguini, M. Laus, P. Dubček, B. Pivac, S. Bernstorff, M. Perego, *ACS Appl. Mater. Interfaces* **2017**, *9*, 11054.

[84] *Physical Properties of Polymers Handbook*, 2nd ed. (Ed: J. E. Mark), Springer Science+Business Media, LCC, New York **2007**.

[85] R. L. Teoh, K. B. Guice, Y.-L. Loo, *Macromolecules* **2006**, *39*, 8609.

[86] S. Walheim, M. Böltau, J. Mlynek, G. Krausch, U. Steiner, *Macromolecules* **1997**, *30*, 4995.

[87] J. Zhang, D. Posselt, A. Sepe, X. Shen, J. Perlich, D.-M. Smilgies, C. M. Papadakis, *Macromol. Rapid Commun.* **2013**, *34*, 1289.

[88] D. Meyerhofer, *J. Appl. Phys.* **1978**, *49*, 3993.

[89] B. A. Fultz, T. Terlier, B. Dunoyer De Segonzac, R. Verduzco, J. G. Kennemur, *Macromolecules* **2020**, *53*, 5638.

[90] W. Brown, in *Dynamic Light Scattering: The Method and Some Applications*, Clarendon Press, Oxford **1993**, p. 177.

[91] C. E. Blanchet, A. Spilotros, F. Schwemmer, M. A. Graewert, A. Kikhney, C. M. Jeffries, D. Franke, D. Mark, R. Zengerle, F. Cipriani, S. Fiedler, M. Roessle, D. I. Svergun, *J. Appl. Crystallogr.* **2015**, *48*, 431.

[92] A. Round, F. Felisaz, L. Fodinger, A. Gobbo, J. Huet, C. Villard, C. E. Blanchet, P. Pernot, S. McSweeney, M. Roessle, D. I. Svergun, F. Cipriani, *Acta Crystallogr., Sect. D: Biol. Crystallogr.* **2015**, *D71*, 67.

[93] D. Franke, A. G. Kikhney, D. I. Svergun, *Nucl. Instrum. Methods Phys. Res., Sect. A* **2012**, *A689*, 52.

[94] B. Hammouda, *J. Appl. Crystallogr.* **2010**, *43*, 716.

[95] J. Teixeira, *J. Appl. Crystallogr.* **1988**, *21*, 781.

[96] SasView, www.sasview.org (accessed: March 2021).

[97] D. Nečas, P. Klapetek, *Cent. Eur. J. Phys.* **2012**, *10*, 181.

[98] H. Amenitsch, M. Rappolt, M. Kriechbaum, H. Mio, P. Laggner, S. Bernstorff, *J. Synchrotron Radiat.* **1998**, *5*, 506.

[99] BornAgain – Software for Simulating and Fitting X-ray and Neutron Small-Angle Scattering at Grazing Incidence, Version 116, https://www.bornagainproject.org (accessed: March 2021).

[100] G. Pospelov, W. Van Herck, J. Burle, J. M. Carmona Loaiza, C. Durniak, J. M. Fisher, M. Ganeva, D. Yurov, J. Wuttke, *J. Appl. Crystallogr.* **2020**, *53*, 262.